HHS Public Access

Author manuscript

Cell Rep. Author manuscript; available in PMC 2019 January 14.

Published in final edited form as:

Cell Rep. 2018 October 30; 25(5): 1158–1170.e9. doi:10.1016/j.celrep.2018.10.022.

Combinatorial Neural Inhibition for Stimulus Selection across Space

Nagaraj R. Mahajan[1] and **Shreesh P. Mysore**[2,3,*]

[1]Department of Electrical and Computer Engineering, Johns Hopkins University, Baltimore, MD 21218, USA

[2]Departments of Psychological and Brain Sciences, and Neuroscience, Johns Hopkins University, Baltimore, MD 21218, USA

[3]Lead Contact

SUMMARY

The ability to select the most salient among competing stimuli is essential for animal behavior and operates no matter which spatial locations stimuli happen to occupy. We provide evidence that the brain employs a combinatorially optimized inhibition strategy for selection across all pairs of stimulus locations. With experiments in a key inhibitory nucleus in the vertebrate midbrain selection network, called isthmi pars magnocellularis (Imc) in owls, we discovered that Imc neurons encode visual space with receptive fields that have multiple excitatory hot spots ("lobes"). Such multilobed encoding is necessitated by scarcity of Imc neurons. Although distributed seemingly randomly, the locations of these lobes are optimized across the high-firing Imc neurons, allowing them to combinatorially solve selection across space. This strategy minimizes metabolic and wiring costs, a principle that also accounts for observed asymmetries between azimuthal and elevational coding. Combinatorially optimized inhibition may be a general neural principle for efficient stimulus selection.

In Brief

Mahajan et al. show that a sparse set of midbrain inhibitory neurons encodes visual space with unusual multilobed receptive fields. This results in a combinatorially optimized solution for selection at all pairs of stimulus locations, which minimizes metabolic and neural wiring costs.

Graphical Abstract

*Correspondence: shreesh.mysore@jhu.edu.

AUTHOR CONTRIBUTIONS

N.R.M. and S.P.M. designed the research, performed experiments, analyzed the data, and wrote the paper.

DECLARATION OF INTERESTS

The authors declare no competing interests.

SUPPLEMENTAL INFORMATION

Supplemental Information includes six figures and can be found with this article online at https://doi.org/10.1016/j.celrep.2018.10.022.

DATA AND SOFTWARE AVAILABILITY

Software code and the data that support the findings of this study are available from the corresponding author upon reasonable request.

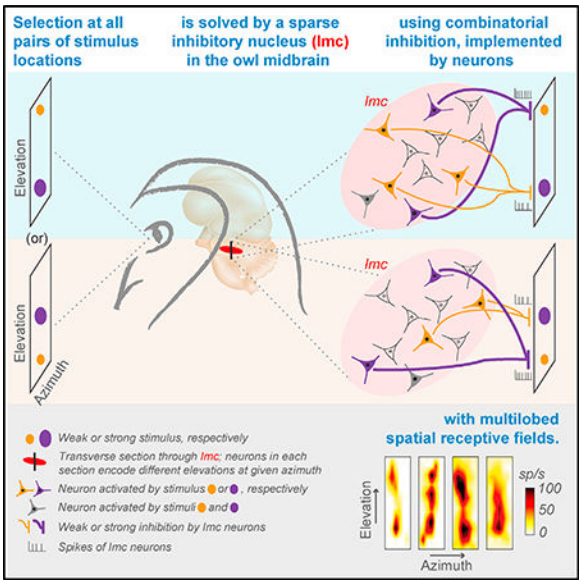

INTRODUCTION

Animals routinely encounter multiple competing pieces of information in their sensory environments. Typically, they handle this informational complexity by selecting the most salient or behaviorally relevant piece of information, i.e., highest “priority” information, to guide their actions (Fecteau and Munoz, 2006; Knudsen, 2007). However, how neural circuits orchestrate the computations that are essential for such stimulus selection is not well understood. Here, we unravel the neural basis of one such critical computation, namely, selection at all possible pairs of locations. This property permits spatial selection to operate no matter which specific locations in the sensory world the competing stimuli occupy. Although appearing straightforward, the implementation of comparisons between all possible pairs of stimulus locations is computationally complex: the number of location pairs at which two competing stimuli could be placed, L^2-L/2, scales quadratically with L, the number of spatial locations that are encoded. How does the brain meet the resulting demands imposed on neural circuitry and solve stimulus selection at all possible pairs of locations?

A brain network with a well-established role in spatial target selection, and therefore an excellent locus to study this question, is the midbrain selection network. It includes the sensorimotor hub, the superior colliculus (SC) (or the optic tectum [OT] in birds), and a satellite inhibitory nucleus called the lateral tegmental nucleus (Graybiel, 1978; Jiang et al., 1996), or isthmi pars magnocellularis (Imc) in birds (Sereno and Ulinski, 1987; Wang et al., 2004) (Figure S1A). The SC/OT, which encodes a topographic map of sensory (and motor) space (Knudsen, 1982; Meredith and Stein, 1986), plays a critical role in stimulus selection across spatial locations. Specifically, the intermediate and deep layers of the SC (SCid) (called OTid in birds) are required for the selection of the highest priority stimulus among distracters (Lovejoy and Krauzlis, 2010; McPeek and Keller, 2004). This selection, which occurs across all possible locations of the competing stimuli, is expressed in the activity of

SCid/OTid neurons as response suppression. When one stimulus is presented at any location, the responses of SCid/OTid neurons encoding that stimulus are suppressed by a competing stimulus presented anywhere outside the neurons' spatial receptive field (RF) (Mysore et al., 2010, 2011; Rizzolatti et al., 1974). The strength of suppression depends on the priorities of the competing stimuli, and is largely independent of their specific spatial locations (Mysore et al., 2010, 2011; Rizzolatti et al., 1974).

Mechanistically, competitive suppression in the OTid is orchestrated by the GABAergic Imc through its specialized anatomical connectivity with the OT (Marín et al., 2007; Mysore and Knudsen, 2013; Wang et al., 2004). Neurons in layer 10 of the OT (OT_{10}) provide input to each Imc neuron, which, in turn, projects back broadly across the OTid space map except to the portions that encode the input locations (Wang et al., 2004) (Figure S1B). This anatomy allows the Imc to implement a spatial inverse operation, distributing priority-dependent inhibition to all competing locations in the OTid space map (Figure S1C). Notably, inactivation of the Imc abolishes this competitive inhibition as well as spatial selection in the OTid (Marín et al., 2007; Mysore and Knudsen, 2013).

In this context, if the spatial RFs of Imc neurons are assumed to be small, resembling those of the input OT_{10} neurons, and possessing the same topographic property as them, a conceptually straightforward strategy by which the Imc might achieve selection for all possible pairs of locations in the OTid is illustrated in Figure S1D. For any given pair of stimulus locations, each stimulus in the pair would activate a group of neighboring Imc neurons encoding for adjacent locations, resulting in inhibition with a spatial pattern that would suppress the neurons encoding the other stimulus (Figure S1D). Simply repeating this Imc-OT circuit module for all location pairs would successfully implement stimulus selection across space with a strategy termed "modular copy-and-paste."

However, the precise nature of the spatial RFs of Imc neurons and their properties are not well understood. Previous work in the Imc suggests that Imc neurons have spatial RFs that are vertically elongated, covering almost the entire extent of elevational space in an uninterrupted manner (Li et al., 2007; Wang and Frost, 1991). If true, such Imc RFs lead to a computational paradox. On the one hand, vertically elongated Imc RFs are unable to implement stimulus selection in the OT at all possible stimulus location pairs: selection cannot be solved for over a third of the location pairs along the elevation (Figure S1E). On the other hand, competitive stimulus selection in the OTid is known to occur across all encoded locations (Mysore et al., 2010, 2011; Rizzolatti et al., 1974), with the Imc being the primary source of competitive inhibition (Marín et al., 2007; Mysore and Knudsen, 2013). To resolve this paradox, we set out to investigate the functional properties of Imc neurons in the barn owl, as well as the computations implemented by the Imc-OT network in service of stimulus selection across space.

Our results indicate that the Imc employs a combinatorially optimized inhibition strategy to solve stimulus selection at all location pairs in the OT. This strategy is supported by an unusual, multilobed encoding of visual space by Imc, one that is consistent with the observed scarcity of Imc neurons available to encode stimulus locations. Although the lobes of individual Imc RFs are distributed seemingly randomly in space, their locations are

optimized across neurons such that assorted but intersecting subsets of Imc neurons are recruited to combinatorially solve selection across two-dimensional (2D) visual space. We show that Imc's combinatorially optimized inhibition strategy for spatial selection minimizes metabolic and neural wiring costs. Moreover, within this framework of neural cost minimization, asymmetries observed in Imc's encoding of elevational versus azimuthal locations are accounted for by asymmetries in its anatomical organization. Together, combinatorially optimized inhibition emerges as an efficient strategy for stimulus selection.

RESULTS

Spatial RFs of Imc Neurons Have Multiple "Lobes"

We measured the visuospatial RFs of Imc neurons using extracellular recordings (STAR Methods). Individual Imc units were identified by spike sorting single and multiunit data; only those units deemed to be of "high quality" were included in the analysis (STAR Methods). Consistent with published data, Imc neurons have high firing rates (median, 76.5 Hz [Goddard et al., 2014; Marín et al., 2007]; Figures 1A, 1B, 1E, and 1F).

We found that individual Imc neurons possessed visual RFs with multiple, distinct response fields or lobes (Figures 1A–1H, S2A, and S2B). The number of lobes in each RF was estimated in an unbiased manner using a two-step process (STAR Methods): (1) a nonlinear clustering method (Rodriguez and Laio, 2014) to fit different numbers of clusters to the spatial map of firing rates followed by (2) a model selection method (Tibshirani et al., 2001) to robustly select the optimal number of clusters in the data (Figures 1C, 1G, and S2C–S2F). We found that about two-thirds of Imc neurons had multilobed RFs (80/116; see also Figure 1L).

To test whether the multilobed structure of Imc RFs was an artifact of our experimental or analytical methods, we performed three controls. First, we tested whether errors in spike sorting might have caused multiple units with single-lobed RFs to be misidentified as a single unit with a multilobed RF. To this end, we applied an additional separability criterion to our sorted units. We tested the statistical separability of the waveforms of each sorted unit with those of any other unit as well as with outlier waveforms recorded at the same site, and retained only those units that were well separated (STAR Methods). We found that the majority of the sorted units (114/116) satisfied the separability criterion as well ($p < 0.05$; Figure 1I), ruling out multiunit contamination as a source of error. Second, we examined whether the spatial sampling resolution used for RF measurement, as well as neuronal response variability, might have caused the erroneous identification of single-lobed RFs as being multilobed (Figure S2G). Using experimentally grounded simulations, we mapped out the values of sampling step size and response Fano factor that yielded a multilobe misidentification rate of 5% or greater (Figure 1J, red zone; STAR Methods). By comparing with experimental data, we found that the values of these parameters from each recorded unit fell outside the 5% misidentification zone. As a final control, because it is well established that OT RFs have single spatial response fields, we measured visual RFs of OT neurons. Our methods correctly identified all of the measured OT RFs as being single-lobed (Figures 1K and S2H). Together, these results confirmed the veracity of our conclusion that the Imc contains predominantly "multilobe" neurons (68%; 78/114; Figure 1L).

RF Lobes Are Distributed along the Elevation, but Not Azimuth

To investigate organizing principles underlying spatial encoding by Imc neurons, we analyzed the properties of the measured visual RFs along the two major anatomical axes of the Imc (Figure S1A). The azimuthal centers of RF lobes were nearly identical for lobes of individual multilobed neurons (Figure 2A, blue data; STAR Methods), across neurons recorded at a given site (Figure 2B, blue data), and across sites recorded along the dorsoventral axis of the Imc (Figure 2C; STAR Methods). However, azimuthal encoding varied systematically along the rostrocaudal axis of the Imc: centers of RF lobes encoded progressively more peripheral azimuths as the recording electrode was moved from rostral to caudal portions of the Imc (Figure 2D; (Li et al., 2007; Wang and Frost, 1991)).

The encoding of elevation by Imc neurons was strikingly different. RF lobes of individual multilobed neurons were spaced arbitrarilyinelevation(Figure 2A:largerangeofreddata).Additionally, RF lobes of multilobed Imc neurons were distributed widely across elevational space: for each multilobed neuron (Figure 2A, inset: large median of data), across neurons recorded at a given site (Figure 2B, red), and across sites recorded along both dorsoventral and rostrocaudal axes (Figures S3A–S3D). There was also no systematic relationship between encoded elevations and distance along either principal axis (Figures S3A and S3B).

These results demonstrated that whereas azimuthal space is encoded in a topographic manner along the rostrocaudal extent of the Imc, elevational space is encoded by RFs with multiple, arbitrarily spaced, and widely distributed lobes of varying number and size (Figures S3E–S3J), with a maximum of three RF lobes per neuron (Figure 1L).

Neuronal Scarcity in Coronal Planes of Imc Necessitates Multiple RF Lobes along Elevation

The multilobed encoding of elevational space by Imc neurons was puzzling. This was especially so because neurons that provide input to the Imc (OT_{10}), as well those that receive Imc's output (OTid), all tile sensory space with single-lobed spatial RFs organized topographically in both elevation and azimuth (Figure 1K) (Knudsen, 1982). Might the implementation of stimulus selection across space, a main function of the Imc (Mysore and Knudsen, 2013), impose demands on the spatial coding properties of Imc neurons that can explain multilobed RFs?

To examine the implications of spatial selection on Imc RF structure and, specifically, of the need for implementing stimulus selection at all possible location pairs, we turned to theory (STAR Methods). Briefly, we compared the total number of location pairs at which selection must occur in the OTid, with the number of location pairs in the OTid at which selection can be achieved by a set of Imc neurons. Since multilobed Imc encoding is restricted along the elevation (Figures 2A, 2B, and S3A–S3D), we focused on stimulus selection between all possible pairs of elevations at any azimuth. We proved mathematically that if the number of Imc neurons (N) encoding different elevations at a given azimuth is less than the number of distinct elevational locations (L) encoded by the OTid at that azimuth ($N < L$), then

multilobed Imc RFs are necessary for stimulus selection at all possible location pairs (STAR Methods).

To examine the biological applicability of this insight, we estimated L and N in the owl brain. For a given azimuth, the OTid encodes elevations ranging typically from-60° to +60°, and does so at a spatial resolution of at least 3° (STAR Methods). Consequently, the number of distinct elevational locations encoded by the OTid at a given azimuth (L_{el}) is at least 120°/3° = 40 ($L_{el} \geq 40$). Next, we estimated the number of Imc neurons encoding these elevational locations (N_{el}). Because visual azimuth is organized topsographically along Imc's rostrocaudal axis (Figure 2D), transverse sections of the Imc provide snapshots of Imc tissue encoding all elevations at a given azimuth (Figures 3A and 3B). We obtained histological sections perpendicular to the rostrocaudal axis of the Imc and performed Nissl staining to visualize cell bodies (STAR Methods). Counts of the number of Nissl-stained somata (García-Cabezas et al., 2016) showed that the majority of sections (75%) had fewer than 28 neurons per section (N_{el}; Figures 3B and 3C). Thus, N_{el} is typically much smaller than L_{el} (median $N_{el}/L_{el} < 26/40 = 0.65$).

In contrast, along the azimuth, N_{az} is greater than or equal to L_{az}. The OTid encodes azimuths ranging typically from −15° to 60° at a spatial resolution of at best 1° (STAR Methods). As a result, the number of distinct azimuthal locations encoded by OTid is at most 75 ($L_{az} \leq 75$). On the other hand, we estimated that there are at least 84 neurons involved in encoding these distinct azimuths, $N_{az} \geq 84$ (STAR Methods). Thus, there are more Imc neurons than there are encoded azimuthal locations ($N_{az} \geq L_{az}$), an observation that is consistent with the absence of multilobed RFs along the azimuth.

These results indicated that multilobed encoding by Imc neurons is consistent with the need for the Imc-OT circuit to achieve stimulus selection at all possible elevational location pairs in the face of a scarcity of Imc neurons encoding elevation (Figures 3B and 3C).

Model Predicts Combinatorially Optimized Inhibition for Selection at All Location Pairs

To explore how an under-complete set of Imc neurons might implement selection at all possible location pairs, we turned to computational modeling. We set up stimulus selection across spatial locations as an optimization problem with L locations (elevations at a given azimuth), and N model neurons encoding those elevations (N < L; Figure S4; STAR Methods). We imbued all model neurons with Imc-like spatially inverting connectivity with the OT (Figures S1 and S4). The spatial RFs of these model Imc neurons were represented, for simplicity, using ones and zeros, with ones corresponding to locations inside the RF, and zeros, outside (Figure 4B; also see Figure S4 for validity of model even when this assumption is relaxed).

The goal of the optimization was to identify the spatial RF structures of these N neurons (i.e., the numbers of their RF lobes and their spatial locations), such that when two stimuli of equal priority were placed at any pair of locations, they suppressed each other equally. This necessary and sufficient condition for implementing selection at all location pairs was captured by a specially constructed cost function whose value decreased as the number of location pairs at which the above condition was satisfied increased. The cost function took

the lowest possible value of –L(L 1) if and only if the condition was satisfied at all location pairs (STAR Methods). Any set of Imc RFs that achieved this minimum value, i.e., that achieved selection for all location pairs, was called an “optimal solution.”

For each value of L, we varied the number of neurons in the model from N = 1 to N = L. In addition, in each case, we examined the impact of single as well as multilobed RFs on the existence and nature of optimal solutions. We did so by including a constraint that specified the maximum number of lobes allowed in a model neuron’s RF, denoted by k_{max}. The values of k_{max} tested were 1, 3, and 10, corresponding to key experimentally relevant values: k_{max} = 1 only permitted model neurons with (traditional) single-lobed RFs as potential solutions to the optimization problem; k_{max} = 3 permitted up to three lobed RFs, in line with the experimental data (Figure 1L); and k_{max} = 10 allowed up to 10 lobes per RF, representing the largest number of typical Imc RF lobes that one can fit within the encoded elevational space (STAR Methods). Therefore, the main parameters in the optimization problem were L (number of locations), k_{max} (maximum number of RF lobes allowed per neuron), and N (number of Imc neurons). For each triplet of (L, $k_{max,}$ N), we ran the optimization problem 1,000 times (Monte Carlo simulation), each time with a different, randomly chosen initial condition, to explore the space of potential optimal solutions.

We found that L = 5 was the smallest number of locations for which selection could be solved at all location pairs with fewer than 5 neurons (Figure 4B). The fewest number of neurons needed by the model in this case, called N*, was 4 (Figure S5A; STAR Methods). Therefore, the maximum “savings” in the number of Imc-like neurons for L = 5 locations was 1 (=L-N*). We found that as L increased, neuronal savings increased (Figure 4A; orange data), with L = 40 locations requiring just N* = 27 neurons to solve selection at all location pairs (savings of 13 neurons or 32%). Neuronal savings also increased as a function of k_{max}, the maximum number of RF lobes allowed per neuron (Figure 4A; black versus orange data). Notably, when only single-lobed RFs were allowed in the model (k_{max} = 1), N* was always equal to L, and there were no neuronal savings (Figure 4A; blue data). Thus, consistent with our theoretical prediction, selection at all possible location pairs could not be achieved with fewer than L neurons if all neurons only had single-lobed RFs.

The primary motivation for our optimization-based modeling approach was to gain insight into the computational logic underlying successful stimulus selection at all possible location pairs when neurons are scarce. An example optimal solution obtained when L = 5 locations, k_{max} = 3 lobes, and N = 4 neurons (Figure 4B), illustrates how fewer than L inhibitory neurons can successfully achieve selection at all location pairs (Figures 4C and 4D). Figure 4E shows another example optimal model solution, obtained when L = 40 locations, k_{max} = 3 lobes, and N = 27 (N*) neurons.

Detailed analysis of optimal model solutions from *all* runs of *all* (L, k_{max}, N) values tested with N < L revealed that every single optimal solution exhibited three functional properties, which we refer to as signature properties. (Figure 5 illustrates these properties for the example optimal solution in Figure 4B and also summarizes them quantitatively for all optimal solutions.) First, every optimal solution contained multilobed Imc neurons (Figures 4B, 4E, and 5A). Conceptually, this “multilobe property” is necessary because of the

scarcity of neurons, i.e., the N < L constraint, as demonstrated previously by theory (STAR Methods).

Second, the RFs of the neurons in optimal solutions collectively exhibited the "optimized lobe overlap" property: every multilobed neuron shared each of its lobes, but not all, with another neuron (Figures 5B–5D). To visualize this property, consider a two-lobed neuron M_a (Figure 5B: for instance, neuron #1 in Figure 4B). There necessarily existed another neuron B (for instance, neuron #2 in Figure 4B) in the solution such that the upper lobe of M_a was shared with the lobes of neuron B, but the lower lobe of M_a was not. Similarly, there also existed another neuron C (for instance, neuron #3 in Figure 4B) in the optimal model solution such that the lower lobe of M_a was shared with the lobes of neuron C, but not the upper lobe. (Here, the neurons B and C could be either single-lobed or multilobed.) This property was quantified using a binary score: briefly, each optimal solution was assigned a score of 1 if every multilobed neuron in that solution satisfied the optimized lobe overlap property (as illustrated in Figure 5B), and 0 otherwise. We found that every optimal solution obtained had a score of 1 (Figure 5C). Conceptually, the optimized lobe overlap property is necessary because selection needs to be solved also when two stimuli are placed at the locations encoded by different lobes of an individual multilobed neuron (Figure 5D). Consequently, this imposes a severe constraint on the relative organization of RF lobes across neurons in optimal solutions—one that causes structured non-orthogonality of the RFs.

Third, neurons in optimal solutions used a "combinatorial inhibition" strategy to achieve stimulus selection at all location pairs (Figures 5E–5J). The combinatorial nature was quantified via a pair of necessary and sufficient conditions, namely that assorted subsets of neurons were selectively recruited to solve stimulus selection for individual location pairs, with the subsets corresponding to different location pairs *intersecting extensively*.

An optimal solution was said to exhibit the assortedness feature if "distant" neurons were recruited to solve selection between even nearby locations (Figures 5E and 5F), and vice versa (Figures 5E and 5G), *no matter* the specific ordering of neurons in the optimal solution (Figure S5B; STAR Methods). This feature was quantified for each optimal solution (STAR Methods): briefly, for a given ordering of neurons in an optimal solution, the selection matrix (as in Figure 4D) was constructed, "nearby" location pairs were identified (STAR Methods), the largest distance between neurons recruited for selection at each nearby location pair computed (STAR Methods), and the maximum value of this "neuronal distance" obtained across all the nearby location pairs in that solution. Then, the minimum value of this neuronal distance was computed across all permutations of neurons within that optimal solution, and across all optimal solutions for that (L, k_{max}, N) triplet (Figure 5F; min-max distance). We found that every optimal solution resulted in the recruitment of distant neurons to solve selection at nearby locations (Figure 5F). Conversely, every optimal solution resulted in the recruitment of nearby neurons to solve selection for distant locations (Figure 5G; max-min distance). These results demonstrated the assorted nature of optimal solutions (see also Figure S6).

An optimal solution was said to exhibit the extensive intersection feature if neural subsets recruited to solve selection even for two location pairs in distant portions of space shared common neurons (Figures 5H and 5I). This feature was quantified by first identifying "doublets": two location pairs such that the locations within each pair were nearby locations, but such that the two pairs themselves occupied distant portions of space. Then we checked whether the neural subsets recruited to solve selection for at least one such doublet involved a common neuron, and scored the solution as 1 if they did (STAR Methods). We found that optimal solutions obtained from all runs exhibited this feature (Figure 5I; see also Figure S6), demonstrating the extensively intersecting nature of optimal solutions. Together, the above results indicated that combinatorial inhibition was a signature property of optimal solutions.

Conceptually, combinatorial patterns of inhibition are a consequence of the RF lobes of model Imc neurons being widely distributed and arbitrarily spaced in the optimal solutions (Figures 5J, S6B, and S6D): restricting RF lobes to only nearby locations substantially limits the number of available RF configurations, potentially precluding optimal solutions. Stated equivalently, the combinatorial *inhibition* strategy arises because of the combinatorial coding of space by the model Imc neurons: individual neurons do not always encode only for neighboring locations (Figures 4B, 4E, S6B, and S6D), and conversely, nearby locations are not always encoded by "nearby" neurons (no matter what permutation of neurons is considered; Figures S5B, S6B, and S6D). Therefore, when two stimuli are presented, two groups of the inhibitory Imc neurons are activated in a nonordered fashion, resulting in a combinatorial pattern of inhibition.

Taken together, the model revealed that selection at all possible location pairs when $N < L$, as is the case with Imc's elevational coding, necessitates a combinatorially optimized inhibition strategy by multilobed neurons.

In contrast, when $N \geq L$, as is the case with Imc's azimuthal encoding, the model was always able to solve selection at all location pairs with just single-lobed neurons (Figure 4A, $k_{max} = 1$, blue data), by using the straightforward modular copy-and-paste strategy (Figure S1D).

Experimental Validation of Model Predictions in Imc

The above modeling results indicated that sparse sets of Imc-like inhibitory neurons use a combinatorially optimized inhibition strategy to achieve selection at all possible location pairs. How-ever, it is unclear whether the owl Imc does, in fact, implement this strategy for selection across elevational locations. To examine this, we tested whether the experimentally recorded activity of Imc neurons exhibited the three signature properties of combinatorially optimized inhibition predicted by the model. Because all elevations at a given azimuth are encoded by neurons within a coronal plane (Figures 2B and 2C), we sampled these neurons by making recordings at multiple dorsoventral sites within each coronal plane (STAR Methods).

Across recordings made in 16 such coronal planes, we found that multilobed neurons were present in nearly every case (14/16; Figure 6A and S3A), thereby validating signature property #1. The impracticability of recording exhaustively from all Imc neurons in a

coronal plane made it infeasible to test whether *every lobe* of each multilobed neuron satisfied the optimized lobe overlap property (signature property #2; Figures 5B–5D). Therefore, we tested whether *at least one lobe* of each multilobed neuron satisfied it (Figure 6B; STAR Methods). The median fraction of multilobed neurons in each coronal plane that satisfied signature property #2 was 1 (Figure 6C).

Finally, we tested for signature property #3 (combinatorial inhibition). Both its features, namely, assorted recruitment and extensive intersection, were satisfied in nearly every testable case (7/8 and 6/6 planes, respectively; Figures 6D–6G; STAR Methods), despite the non-exhaustive sampling of Imc neurons in individual planes. In addition, the computational basis of combinatorial inhibition, namely, combinatorial coding of space by model Imc neurons, which was quantified via the arbitrary spacing and wide distribution of their RF lobes (Figure 5J), was also found in experimental data (Figures 2A, 2B, and S3A–S3D).

Thus, our experimental results show that owl Imc neurons are activated in a combinatorially optimized fashion that solves stimulus-priority-dependent competitive selection across location pairs in the OT.

DISCUSSION

This study unpacked the mechanistic underpinnings in owls of a critical neural function, namely stimulus selection at all location pairs, and revealed combinatorially optimized inhibition as an efficient strategy for it when neurons are scarce. Combinatorial activation of neurons is typically inferred by visualizing their patterns of activation in response to stimuli; for instance, combinatorial activation of odors by olfactory receptor neurons (Sicard and Holley, 1984). Here, in addition to visualizing these patterns, we quantified the underlying intuition by defining the “assortedness” and “extensive intersection” features, which are necessary and sufficient for combinatorial activation, and applied this approach to both model solutions as well as experimental data. This allowed for quantitative support for the finding of combinatorially optimized activation of inhibitory neurons. Broadly, this study was framed in the context of selection between pairs of stimulus locations. However, because selection between more than two stimuli requires comparisons between all the possible stimulus pairs, the results of this study apply directly to the general problem of selection among any number of competing stimuli.

Multilobed Visuospatial RFs and Stimulus Selection

Multilobed spatial RFs have not been reported previously in any early visual area to the best of our knowledge. We found that, in the Imc, a sensory area that is just two synapses away from the retina (Wang et al., 2006), the majority of neurons have multilobed visual RFs. This contrasts with previous reports of large, vertically elongated visual RFs in the Imc (Li et al., 2007; Wang and Frost, 1991), a consequence of the detailed approaches used here, rather than species differences (Marín et al., 2007). Multilobed Imc RFs were characterized here using flashing dots as visual stimuli. The use of this classical approach, which has been employed extensively in visual neuroscience, highlights the contrast between the unusual multilobed encoding of space by Imc and the traditional single-lobed encoding of space by other early visual areas including OT (Figure 1K).

Imc does not play a functional role in OT's representation of the features of single stimuli (Mysore and Knudsen, 2013). In contrast, Imc plays a critical role in delivering global competitive inhibition across the OT space map and enables the selection of the highest priority stimulus by the OT (Marín et al., 2007; Mysore and Knudsen, 2013). Therefore, potential functions for Imc's multilobed RFs were best considered in the context of competitive stimulus selection across space, rather than in the context of neural or behavioral responses to single stimuli. In so doing, we showed that the scarcity of Imc neurons available to encode elevational locations at a given azimuth necessitated multilobed RFs in order to achieve stimulus selection across elevations (in that azimuthal plane).

Stimulus Selection across Space and Model Assumptions

Through computational modeling and subsequent experimental validation, our results showed that the multilobed RFs of sparse Imc neurons implement a combinatorial inhibition strategy for solving stimulus selection across locations (Figure 4). Our model included three key biological properties of the Imc-OT circuit as axiomatic features: (1) that Imc neurons are scarce (in elevation); (2) that they interconnect with the OT in a specialized, spatially inverting manner; and (3) that selection along elevation in the OT depends entirely on the priorities of the competing stimuli but not on their specific locations. The first axiomatic feature was demonstrated in Figure 3. The second, although not yet confirmed functionally, is consistent with anatomical tracing studies (Wang et al., 2004). The third, invariance of competitive suppression along elevation, has been demonstrated in previous work (Mysore et al., 2010). Incidentally, in other species, there are asymmetries between upper and lower hemifields (Yilmaz and Meister, 2013), and more generally, there can be a spatial gradient with stimuli at different locations being weighted differently; such a weighting function is easily incorporated into our optimization model.

As the goal of our modeling was to extract core computational principles underlying the implementation of selection at all location pairs, we chose, in the interest of model simplicity, not to include other details of Imc RFs observed in the data (Figure S3) beyond the three axiomatic features. These included proportions of single versus multilobed RFs, the relative spreads of the heights of single- versus two- versus three-lobed RFs, etc. In addition, the model made two other simplifying assumptions. First, to reduce model complexity, model RFs were implemented as discrete, binary "pixels" (Figure 4), as opposed to being continuous hills of activity (Figure 1). As described in Figure S4, this assumption does not affect the spatial pattern of Imc inhibition onto the OT. However, it fails to capture the scaling of the strength of the inhibition based on the specific position of the stimulus within the half-max extent of a RF. Second, the model implemented the biological observation that the maximum number of lobes in any Imc RF (denoted k_{max}) was three (Figure 1L) by constraining the number of RF pixels to be less than or equal to $k_{max.}$ The consequence of this assumption was that the sizes of model RFs were also limited to k_{max} pixels (Figures 5E, S5B, and S6BD; $k_{max} = 3$), unlike biological RFs that could be larger in size (Figures 1, 6, and S2). This assumption was nonetheless necessary because it improved the convexity of the cost function, thereby allowing the runs of the optimization model to converge. Despite these assumptions, however, strong predictions of the model regarding combinatorially optimized inhibition for location-invariant selection (and the corresponding

signature properties) were successfully validated with subsequent experiments, demonstrating that the Imc does indeed employ combinatorially optimized inhibition for stimulus selection at all possible elevational pairs.

Notably, the signature properties were also robust to the specific proportions of single- versus two- versus three-lobed RFs. This was evidenced by the fact that, in the model, the signature properties held true for all optimal solutions even though the proportions of lobes varied widely across optimal solutions: for instance, one of the optimal solutions for L = 40, N* = 27 consisted of 7.5% single-lobed, 18.5% two-lobed, and 74% three-lobed RFs, whereas one optimal solution for L = 5, N* = 4 consisted of 50% single-lobed, 25% two-lobed, and 25% three-lobed RFs (Figure 4B). Consequently, our conclusions were not impacted by a match (or not) between proportions of RFs in the model Imc and the proportions in the owl Imc. (Incidentally, because the proportions in experimental data were obtained, necessarily, by combining data across coronal planes and across birds, they do not represent the distribution within any particular Imc coronal plane [Figure 1L].)

Selection across Locations in Elevation versus Azimuth

Our results indicate that the Imc implements stimulus selection for locations both along elevation and azimuth. However, the strategy employed for location pairs along the elevation is distinct from that along the azimuth, a difference that can be accounted for by the difference in anatomical organization along the two axes. The scarcity of Imc neurons in coronal planes is consistent with a combinatorially optimized solution for selection along elevational locations through the use of multilobed spatial RFs (Figures 3, 4, 5, and 6). In contrast, abundance of Imc neurons along the rostrocaudal axis (STAR Methods) is consistent with the modular copy-and-paste solution through the use of single-lobed spatial RFs (Figure S1D).

Minimization of Wiring and Metabolic Costs

In this context, three questions regarding the biological implementation of selection at all location pairs by the Imc remain puzzling. First, why might N < L be biologically desirable in the Imc in the first place, necessitating combinatorially optimized inhibition? Second, if N < L is attractive biologically, why do Imc RFs not have a large number of lobes, thereby achieving greater savings in the number of Imc neurons (Figure 4A)? In other words, why is the maximum number of Imc RF lobes restricted to a low number (k_{max} = 3; Figure 1L)? Third, why is multilobed encoding found only along one spatial axis (here, elevation), and why not along both axes for greater neuronal savings?

To gain insight into these questions, we examined Imc function in the context of two types of costs that nervous systems must incur in building and operating a neural circuit: wiring cost and metabolic cost. We estimated wiring cost by quantifying the cost of implementing spatially inverting projection patterns from the Imc to the OT (Chen et al., 2006), and metabolic cost by quantifying the cost of broadcasting of spikes across the OT for competitive suppression. We found that wiring cost decreases as the number of RF lobes increases (Figure 7A; STAR Methods). In contrast, metabolic cost increases as the number of RF lobes increases (Figure 7B; STAR Methods). Consequently, the wiring cost places a

lower bound on the number of RF lobes (and a corresponding upper bound on the number of neurons), whereas the metabolic cost places an upper bound on the number of RF lobes (and a lower bound on the number of neurons). The optimal number of RF lobes (and the number of neurons necessary), therefore, is one that minimizes some weighted combination of the two opposing costs (Figure 7C). Because Imc neurons have high firing rates (median, 76.5 Hz [Goddard et al., 2014; Marín et al., 2007]; Figure 1A), this causes the metabolic cost of Imc function to scale up substantially, pulling the ideal number of RF lobes to even lower values than for low firing-rate neurons (Figure 7C, thick versus thin line; thereby also providing a rationale for the continued presence of some single-lobed neurons in the Imc; Figure 1L).

Taken together, these results indicate that a small number of Imc neurons ($N < L$), with multilobed RFs that have a small number of RF lobes (small k_{max} value), are well suited to achieve selection across all locations if net neural costs are to be minimized. Increasing excessively the number of RF lobes along one spatial axis (here, elevation), or increasing the number of RF lobes also along the other axis as well (here, azimuth) are not biologically desirable. Thus, the estimation of the net cost of neural circuit operation provides a plausible window into “why” the owl Imc may be organized functionally in the way that it is (Figure 7).

The reason for occurrence of multilobed encoding along elevation, specifically, rather than along azimuth, is less evident and may simply be a consequence of the relative anatomy of Imc and OT. The Imc is asymmetric in shape, elongated along the rostrocaudal axis, but compressed along the dorsoventral axis (Wang et al., 2004). It is plausible that the OT’s representation of azimuth along its rostrocaudal axis (Knudsen 1982) drives azimuths to be encoded along the parallel (and neurally rich) rostrocaudal axis of the Imc (Wang et al., 2004), for ease of wiring, thereby relegating elevation to be coded by the transverse (and neurally sparse) planes.

Space Coding in Imc Is Unlike Traditional Population Coding Schemes

The multilobed encoding of space by Imc neurons (Figures 1, 6, and S6) combined with the optimized lobe overlap (signature property #2; Figures 5 and 6) across Imc RFs in a coronal section, led to the observation that Imc neurons use a combinatorially optimized population coding strategy (Figures 6 and S6). This coding is conceptually distinct from the major population neural coding schemes described thus far in the literature.

For instance, in population vector coding, multiple neurons with overlapping, single-lobed tuning curves (or RFs) are activated to encode feature values such as stimulus locations, motion direction, etc., with high precision (Georgopoulos et al., 1986; Lee et al., 1988; Lewis and Kristan, 1998; Ma et al., 2006). With such coding, it is always possible to order these RFs along the feature axis such that neighboring values of features are always encoded by functionally “local” subsets of neurons (Figures S6A and S6C). In contrast, neurons with multilobed RFs cannot be ordered this way: some neurons always code also for distant locations (Figures S6B, S6D, and 5J), and selection for a given location pair cannot be guaranteed to be solved by only a local subset of neurons (Figures S6B and S6D).

A population coding scheme reported in the literature that does involve multilobed encoding as well as the activation of non-local neural subsets is the combinatorial coding of odors by olfactory receptor neurons (Sicard and Holley, 1984). However, whereas assorted and extensively intersecting subsets of neurons are activated to encode odors, no inherent constraints that necessitate the optimization of the relative positioning of these RF lobes across neurons have been reported. In contrast, in the combinatorially optimized coding reported here, the placement of RF lobes needs to be optimized across neurons and is exemplified by the lobe overlap property (Figure 5B and 5C).

For this same reason, our scheme also differs from the encoding of space by entorhinal grid cells: the firing fields of different grid cells are not inherently yoked to one another (Hafting et al., 2005; Towse et al., 2013). In addition, each grid cell has a large number of highly organized firing fields, unlike the few, and arbitrarily placed, RF lobes of Imc neurons.

Finally, combinatorially optimized coding also stands in direct contrast to the sparse, orthogonal coding by an overcomplete set of neurons reported in many brain areas (Mao et al., 2017; Olshausen and Field, 1997). Imc's coding, instead, involves promiscuous, non-orthogonal representation of space by an undercomplete set of neurons.

The problem of stimulus selection at all location pairs with limited neurons, which yields combinatorially optimized coding in Imc, belongs to the same (np-complete) class of computationally complex problems as the traveling salesman problem and the minimum spanning tree problem (Kruskal, 1956; Lawler et al., 1985). Although the brain solves this problem naturally, exactly how Imc's optimized, multilobed RFs are specified during neural development is an intriguing open question and a subject for future work.

Generality of Combinatorially Optimized Coding beyond the Owl and the Imc

The discoveries, here, of multilobed visual representation, combinatorially optimized population coding, and an efficient inhibitory solution for a critical brain function (namely, stimulus selection) have come from the systematic study of the functional response properties of inhibitory neurons in the owl Imc, an area proposed as a critical processing critical processing hub for stimulus selection for attention (Marín et al., 2007; Mysore and Knudsen, 2013; Sereno and Ulinski, 1987).

Although Imc is conserved across the midbrain of all vertebrates (Graybiel, 1978; Jiang et al., 1996; Wang et al., 2004), the functional properties of this nucleus of emerging importance have not been studied in any vertebrate other than the barn owl thus far. The biological advantages of the unusual coding strategy elucidated here suggest that combinatorially optimized coding by sparse inhibitory neurons may be a solution employed generally by the vertebrate midbrain to achieve spatial selection across all locations.

Additionally, this computational strategy extends naturally to any selection problem in which the choice must be made no matter what the specific values are of other stimulus features such as orientation, color, odor identity, etc. One example is feature-based pop-out (Treisman and Gelade, 1980), in which, for instance, a bar-shaped visual stimulus of a particular orientation stands out (is "selected" neurally and behaviorally) among a

background of several bars of a different orientation. Since pop-out must and does operate effectively *no matter* what the absolute orientations of the bars are (as long as their relative orientations are distinct), the underlying circuit mechanism must have the ability to compare responses of neurons encoding for different, and in fact, all possible, pairs of orientations, much like the Imc helps compare responses of OT neurons encoding for different (all possible pairs of) locations. Our results suggest that a careful examination of the encoding properties of inhibitory neurons in cortical as well as sub-cortical areas may reveal combinatorially optimized coding as a widespread strategy in the brain for efficient, feature-invariant stimulus selection and decision making under metabolic and anatomic constraints.

STAR⋆METHODS

KEY RESOURCES TABLE

REAGENT or RESOURCE	SOURCE	IDENTIFIER
Experimental Models: Organisms/Strains		
Adult barn owls (*Tyto alba*)	Johns Hopkins University, Stanford University, University of Maryland	N/A
Software and Algorithms		
Custom code for RF analysis and computational modeling in MATLAB	This paper	N/A
Gap statistical analysis for model selection	Tibshirani et al., 2001	In-built MATLAB function (‘evalclusters’)
MIDACO-SOLVER (Solver for nonlinear optimization problems)	Schlueter et al., 2012	http://www.midaco-solver.com/
Clustering by fast search-and-find of density peaks (for clustering RF data)	Rodriguez and Laio, 2014	https://people.sissa.it/~laio/Research/Res_clustering.php

CONTACT FOR REAGENT AND RESOURCE SHARING

Further information and requests for resources and reagents should be directed to and will be fulfilled by the Lead Contact, Shreesh P. Mysore (shreesh.mysore@jhu.edu).

EXPERIMENTAL MODEL AND SUBJECT DETAILS

Animals—We performed experimental recordings in 15 head-fixed, non-anesthetized adult barn owls that were viewing a visual screen passively (*Tyto alba*). Both male and female birds were used; the birds were shared across several studies. All procedures for animal care and use were carried out following approval by the Johns Hopkins University Institutional Animal Care and Use Committee, and in accordance with NIH guidelines for the care and use of laboratory animals. Owls were group housed in enclosures within the aviary, each containing up to 6 birds. The light/dark cycle was 12 hr/12 hr.

METHOD DETAILS

Neurophysiology—Experiments were performed following protocols that have been described previously (Mysore et al., 2010; Mysore and Knudsen, 2013). Briefly, epoxy-coated, high impedance, tungsten microelectrodes (A-M Systems, 250μm, 5–10 MΩ at 1 kHz) were used to record single and multi-units extracellularly. A mixture of isoflurane (1.5%–2%) and nitrous oxide/oxygen (45:55 by volume) was used at the start of the experiment to anesthetize the bird and secure it in the experimental rig (a 30-minute period of initial set-up). Isoflurane was turned off immediately after the bird was secured and was not turned back on for the remainder of the experiment. Frequently, nitrous oxide was also turned off at this point, but in several experiments, it was left on for a few hours if needed. However, it was turned off at least 30 minutes before the recording session. Our recordings were performed starting, typically, 3 hours after initial set-up (the time required for positioning the electrode). As recovery from isofluorane occurs well under 30 minutes after it is turned off, and recovery from nitrous oxide occurs within a minute (the bird stands up and flies away if freed from restraints), recordings were made in animals that were not anesthetized and non-tranquilized.

Imc targeting—The Imc is an oblong structure that is 2.8 mm rostrocaudally and 0.35 mm dorsoventrally, appearing as a 700-μm × 350-μm elliptical disk in coronal sections. It lies parallel to the rostrocaudal axis of the OT, located approximately 16 mm ventral to the surface of the brain, and approximately 500 um medial to the medial-most part of the OT. We targeted the Imc following previously published methods (Mysore and Knudsen, 2013). Briefly we first navigated to the OT (based on well-established methods; (Knudsen, 1982)), and then navigated to the Imc using the OT's topographic space map as reference. Imc targeting has been validated previously using dye injections (Mysore and Knudsen, 2013), and was additionally verified at the outset of this study through anatomical lesions (Figure S1A). Dorsoventral penetrations through the Imc were made at a medial-leading angle of 5° from the vertical to avoid a major blood vessel in the path to the Imc.

Visual stimuli and RF measurement—Visual stimuli used here have been described previously (Mysore et al., 2010, 2011). Briefly, stationary, translating, or looming visual dots (of fixed contrast) were flashed at different locations on a tangent TV monitor in front of the owl. Looming stimuli were dots that expanded linearly in size over time, starting from a size of 0.6°in radius. Visual stimuli were presented for 250ms with an inter stimulus interval of 1.5–3 s at all sampled locations. Pilot experiments indicated that visual RFs were narrow in azimuth but spread along the elevation. Therefore, RF measurements were made by presenting stimuli over the −60° to 60° range in elevation, and over a 40°(±10.4°) range in azimuth (centered around the azimuth that yielded the best responses). The ranges of sampling steps used were 4°−10°in azimuth and 5°−15°in elevation. Typically, we sampled 55–70 spatial locations for each neuron (typically, 6 locations along azimuth and 10 locations along elevation). Each sampled stimulus location was repeatedly tested 9–15 times in a randomly interleaved fashion. Multi-unit spike waveforms, recorded using Tucker Davis Technologies hardware interfaced with MATLAB, were sorted offline into putative single neurons (see below). The spatial responses for each neuron were measured by counting spikes at each sampled location during a 100–350 ms time window following stimulus onset.

Spike sorting multi-unit data—The '*chronux*' spike-sorting toolbox was used for the majority of the analyses (Fee et al., 1996). This method is based on a hierarchical unsupervised clustering approach in which the spike waveforms are initially classified into a large number of clusters, typically 10 times the number of putative units recorded. Clusters with very few spikes are discarded and the remaining clusters are then aggregated automatically using metrics of similarity between waveform shapes. In addition, we include only those units for analysis that have less than 5% of the spikes within 1.5 ms of each other (ISI criterion).

The statistical separability of individual sorted units was assessed based on the distance of a unit's cluster (of waveforms) from the clusters corresponding to other units as well as the outlier cluster measured at the same site. We first projected the spike waveforms measured at a given site to a 3-dimensional space using principal components analysis. Then, we performed a one-way ANOVA test to examine if the mean of the waveforms of a given unit (in the projected 3-dimensions) was significantly different from the means corresponding to the other units and the outliers. This was followed by the Holm-Bonferroni criterion for multiple comparisons. In a few cases (4/116), there were either too few waveforms in the outlier cluster (number of waveforms in outlier cluster less than 8% of number of waveforms in any of the remaining sorted units), or the outlier waveforms did not form a cluster with a Gaussian distribution. In such cases, we only tested for the distance of the unit's cluster mean from the cluster means of other units. We regarded only those units whose cluster means were significantly different from the means of all other units (and the outlier cluster) as 'well-separated' units per this separability criterion ($p < 0.05$; the p value plotted for each unit in Figure 1I is the largest p value obtained across all comparisons for that unit). Only well-separated units were included in all remaining analyses (subsequent to Figure 1I) in this study.

Identification of the optimal number of RF lobes (Figure 1)—In order to determine the number of response fields (or lobes) in an RF in an unbiased manner, we first transformed the measured RF responses to a distribution of points in 2-dimensional space (azimuth x elevation). This distribution was generated such that the density of points around each sampled spatial location was proportional to the firing rate of the neuron evoked by a visual stimulus presented at that location. We achieved this by distributing points randomly and uniformly within a rectangle centered around the sampled location such that the number of points was equal to the firing rate at that location; the dimensions of the rectangle were the azimuthal and elevational sampling steps, respectively. This transformation allowed us to apply spatial clustering methods to the firing rate maps.

Next, using the density peaks clustering method (Rodriguez and Laio, 2014), we fit successively k = 1,2,3.6 clusters to the distribution (Figures 1C and 1G). This clustering method identifies cluster centers by searching for regions that have high local density of points (r) that are also far away from any points of equal or higher density (δ = minimum distance from points of equal or higher density; Figures S2C–S2F. For the point with highest local density, δ is conventionally taken as the maximum distance of the point from all other points). It is robust to nonlinear cluster boundaries and unequal cluster sizes – conditions under which traditional methods like k-means perform poorly. The k cluster centers are

chosen by the algorithm as points with the k highest values of gamma (γ), defined as the product of ρ and δ. We repeated this procedure for each k, thereby fitting the 1-best, 2-best, … 6-best clusters to the data.

Following this, we applied a model selection procedure to identify the optimal number of clusters in the data, i.e., the best k value (k*), based on the 'gap statistic' (Tibshirani et al., 2001). This is an unbiased method to detect the number of clusters that best fit a distribution of points. For each k, we estimated a 'gap' value (*gap(k)*), which evaluated the goodness of fitting k clusters to the distribution. The gap value was calculated by standardizing the pooled within-cluster sum of square distances between all points in each of the k clusters (W_k) and comparing its log value (log (W_k)) to the expectation of this quantity, (E*(log (W_k)), under the null hypothesis that the data contains only one cluster (Tibshirani et al., 2001). We calculated this in MATLAB by using the '*evalclusters*' function with '*gap*' as the evaluation method, which yielded *gap*(*k*) as well as *se*(*k*) for each k; *se*(*k*) was the standard error in the estimate of *gap*(*k*). Then, the gap selection statistic was defined as, *GAP(k)* = *gap(k)- gap(k+1) + se(k+1)*. The number of clusters that fit the data optimally is defined by the method as the smallest value of *k* for which *GAP(k)* > = 0. Conceptually, the value of *GAP(k)* for the null hypothesis (*k** = 1) keeps decreasing linearly with increasing *k*, whereas the rate of the decrease of the metric under the alternate hypothesis (*k** > 1) has been shown to fall exactly at *k* = *k**. Hence the '*gap*' between the two curves is maximum at *k* = *k**, and *GAP(k)*, the difference between *gap(k)* and *gap(k+1)* is greater than zero for the first time when *k* = *k**.

Defining the centers of RF lobes—The center of an RF lobe defined as the stimulus location evoking the highest firing rate within that lobe. The azimuthal RF 'center' of an Imc neuron is defined as the average of the azimuthal centers of all of its RF lobes, because RF lobes of an individual neuron do not vary significantly in azimuth (Figure 2A; blue). The azimuthal RF 'center' of a recording site in the Imc, across all the neurons recorded at that site, is defined as the average of the azimuthal centers across all the RF lobes of all the neurons recorded at that site. This is valid because RF centers of individual neurons within a recording site do not vary significantly in azimuth (Figure 2B; blue). The azimuthal RF 'center' of a penetration is defined as the average of the azimuthal centers across all recording sites in that penetration. This is valid because RF centers of individual recording sites within a penetration do not vary significantly in azimuth (Figure 2C).

Monte-Carlo analysis of the effect of neuronal noise and spatial sampling resolution on number of detected RF lobes (Figure 1)—A low spatial sampling resolution during the measurement of spatial RFs, as well as high variability in neural responses, could both cause a single lobed RF to appear falsely as a multilobed one (see Figure S2G). To test how robust our method for identifying the ideal number of RF lobes is to sampling resolution (sampling step-size) and neural response variability (response Fano-factor; defined as variance/mean), we performed the following control. First, we generated a single-lobed Gaussian in 2D (azimuth x elevation), with mean and covariance equal to the average values of these parameters across all the experimentally measured Imc RFs (114 Imc units). Using this single-lobed RF as 'reference', we repeatedly simulated RFs using

different step-sizes and different response Fano-factor values: For a given step-size, the firing rate at each location was chosen randomly from a normal distribution with mean equal to the value yielded by the reference RF at that location, and variance determined by the Fano-factor value. Next, we transformed this simulated RF into a distribution of 2-D points and applied the density peaks clustering method. Finally, we applied the gap-statistic model selection method to determine the ideal number of lobes in the RF. We repeated this 150 times for each step-size and Fano-factor pair, and calculated the fraction of times for which multiple RF lobes were detected (erroneously) in this data. We repeated the whole procedure for a range of step-size and Fano-factor values that subsumed the range of experimental step-sizes and measured Fano-factor values, and identified the zone that yielded ≥ 5% false detection rate of multiple lobes (Figure 1J).

To test the extent to which our experimental and analytical methods falsely detected multilobed RFs, we compared the experimentally used step-size for each RF and the RF's Fano-factor value with those that yielded a ≥ 5% false detection rate in simulation. The Fano-factor for each RF was calculated as the average of the Fano-factor values at all sampled locations in that RF. The step-size for each RF was calculated as the average of the azimuth and elevation sampling steps used to measure the RF. We found that all of our RFs were well within the 'safe' zone of ≤ 5% error (Figure 1J). Thus, the detection of multilobed RFs in our data was unlikely to be a spurious consequence of sub-optimal measurement conditions.

Histology (Figure 3)—Owls were perfused with paraformaldehyde and their brains extracted per standard procedures. The fixed brains were blocked so that the rostro caudal axis of the Imc was perpendicular to the sectioning plane, and brain sections of 40μm thickness were obtained. Sections containing Imc were mounted, Nissl stained, and coverslipped. Sections were imaged at 40x under a light microscope and the number of Nissl stained somata in the Imc in each section were manually counted by NRM and SPM independently (García-Cabezas et al., 2016). For each section, the maximum value of the counts from the two authors was used to generate the plot in Figure 3C.

Theoretical calculations regarding the need for multilobed RFs—We compared the total number of location-pairs at which selection must occur in the OTid, with the number of location-pairs at which selection is achievable by a set of Imc neurons. Since multilobed Imc encoding is restricted along the elevation (Figures 2A and 2B), we focused on stimulus selection between all possible pairs of elevations at any azimuth.

Simplified version.: We started by making two simplifying assumptions: (a) that the OT space map is a collection of non-overlapping spatial RFs that tile sensory space, and (b) that each Imc neuron has exactly k RF lobes (k always ≥ 1).

In this scheme, if the number of distinct elevations (at a given azimuth) in the discretized OT space map is L, then the total number of distinct pairs of stimulus locations possible is $L(L-1)$. A stimulus placed within any RF lobe of a k-lobed Imc neuron can suppress competing stimuli located anywhere outside the RF, i.e., at $L-k$ locations. Therefore, each Imc neuron is capable of implementing competitive selection at $k(L-k)$ pairs of locations.

With N such Imc neurons, the number of pairs of stimulus locations at which competitive selection can be resolved by the Imc is at most $Nk(L-k)$. Note that this quantity is computed assuming no overlap between Imc RFs and is greater than the number of pairs of stimulus locations at which competitive selection can be resolved by the Imc if overlap between RFs is allowed. Therefore, to achieve successful competitive suppression between all possible pairs of stimulus locations, i.e., location invariance, a condition that must be satisfied is

$$Nk(L-k) \geq L(L-1) \quad (1)$$

$$= > k \geq \frac{L(L-1)}{N(L-k)} \quad (2)$$

This necessary (but not sufficient) condition for location invariance is already very revealing: If all Imc neurons had only single-lobed RFs, i.e., $k = 1$, the above inequality reduces to $N \geq L$ i.e., the number of Imc neurons would need to be greater than or equal to the number of distinct spatial locations. Since the logical proposition 'A = > B' is exactly the same as the proposition 'not (B) = > not (A)', in our case, the proposition 'k = 1 = > N ≥ L' is exactly the same as the proposition 'N < L = > k≠1', i.e., if the number of Imc neurons is less than the number of spatial locations, then at least one Imc RF must be multilobed (because RFs cannot have fewer than one lobe, by definition).

This conclusion held true even when both the simplifying assumptions – (a) that OT RFs are non-overlapping, and (b) that all Imc neurons have the same number of RF lobes – were relaxed (see 'Full version' next).

Full version.: We used a more biologically accurate model of space in which RF extents, overlap of RFs across neurons, and the resolution of competition reported in the OTid (the minimum distance between two stimuli such that OTid is able to select the stronger of the two stimuli) (Mysore et al., 2010) were all modeled to match experimental data. In addition, we allowed varying numbers of Imc RF lobes:

Let the total range of elevational locations for which barn owl's midbrain encodes space be R, and the resolution of encoding space be r. Then, the number of distinct locations at which a stimulus can be placed along elevation is $L = R/r$. Let the resolution for competitive selection be C_{res}.

The total number of distinct location-pairs at which two competing stimuli can be placed such that they are greater than C_{res} apart from each other is approximately $L(L - (2Cres/r))$. Note that this quantity is calculated by counting all the locations at which a second stimulus can be placed such that it is at least C_{res} away on either side of a first stimulus that is placed in any of the L locations. However, when a first stimulus is placed at the edge of the visual field, a second competing stimulus can be placed only on one side such that it is C_{res} away. It is straightforward to show that $L(L - (2Cres/r))$ is smaller than the corresponding quantity obtained when edge effects are included. Hence, for location invariance to be achieved,

selection of the stronger stimulus must at least be implemented when two competing stimuli are placed in any of these possible location-pairs.

Let the number of lobes in a given Imc neuron be k. Let the half-max size of each lobe be l_h. Then, a k lobed Imc neuron solves competition for a total of $k(L-(l_h/r)k)$ location-pairs (assuming each Imc neuron sends inhibition to all locations that lie outside the half-max extent of the neuron's RF, without loss of generality; see "Model assumptions" section below and Figure S4 for implications of this assumption). This is just the number of location-pairs such that one stimulus can be placed inside the multilobed RF (at its peak for effective suppression of competing stimuli) and the other outside. Let the total number of k lobed Imc neurons be N_k. Therefore, the total number of Imc neurons is

$$N = \sum_k N_k k \quad (3)$$

To achieve location invariance, we need

$$\sum_k N_k k\left(L - \frac{I_h}{r}k\right) \geq L\left(L - \frac{2C_{res}}{r}\right) \quad (4)$$

Since $k \geq 1$, and $l_h > 2C_{res}$ (mean $l_h = 33.6° \pm 1.25°$ from the 209 RF lobes across 114 Imc neurons we measured, and $C_{res} < 10°$ (Mysore et al., 2010)), we get

$$\left(L - \frac{I_h}{r}k\right) \leq \left(L - \frac{2C_{res}}{r}\right) \quad (5)$$

Using (5) in (4) gives,

$$\sum_k N_k k \geq L \quad (6)$$

In other words, if all the Imc neurons are single-lobed (k = 1), this equation becomes $N \geq L$. Since the logical proposition 'A = > B' is exactly the same as the proposition 'not (B) = > not (A)', the proposition '$k = 1 = > N \geq L$' is exactly the same as the proposition '$N < L = > k \neq 1$' i.e., if the number of Imc neurons is less than the number of spatial locations, then at least one Imc RF must be multilobed (because RFs cannot have fewer than one lobe, by definition).

Estimating number of elevational and azimuthal locations encoded by OTid (L_{el} and L_{az}, respectively)—To estimate, conservatively, the number of distinct elevational locations encoded by the OTid, we divided the extent of elevational space by the poorest resolution of spatial encoding by OTid neurons. The OTid encodes elevations ranging typically from −60°to 60°(Knudsen, 1982; Mysore and Knudsen, 2013). The poorest

OTid spatial resolution was estimated as the largest distance between adjacent spatial locations for which discriminability (d-prime) of neural responses was above a plausible threshold of 1(Bala et al., 2003). Using published data (Sridharan et al., 2011) that reports d-prime values computed from spatial tuning curves in the OTid, we estimated the OTid's poorest spatial resolution at 3°. Thus, the number of distinct elevational locations encoded was at least 120°/3°, in other words, $L_{el} \geq 40$.

To estimate the largest number, the number of distinct azimuthal locations encoded by the OTid, we divided the extent of azimuthal space by the best resolution of spatial encoding by OTid neurons. The OTid encodes azimuths ranging typically from −15° to 60(Knudsen, 1982; Mysore et al., 2010). In addition, the OTid encodes frontal azimuths with a magnification factor of 150 μm/deg, and peripheral azimuths with a magnification factor of 50 μm/deg (Knudsen, 1982). Because resolution varies inversely as the magnification factor, we estimated the best spatial resolution from the poorest using M-scaling 3°* 50/150 = 1° (Carrasco and Frieder, 1997). Thus, the number of distinct azimuthal locations encoded was at most 75°/1°, in other words, $L_{az} \leq 75$.

Selection across azimuthal locations—The number of distinct azimuthal locations encoded by OTid was estimated above to be ≤ 75 ($L_{az} \leq 75$).

The rostrocaudal extent of the Imc is 2800 μm, and the somas of Imc neurons are no larger than 33 μm (largest somatic dimension = 33 μm, n = 456 neurons across 20 coronal sections). Therefore, there are at least 84 (coronal) sections along the rostrocaudal axis of the Imc (2800/33), with each section containing at least one Imc neuron not also found in the neighboring sections. (For this conservative estimate of N_{az}, we only need that of the ~26 neurons in each successive coronal section of the Imc (median #neurons per section = 26; Figure 3C; dashed red line), just one be distinct.) In other words, there are at least 84 neurons involved in encoding the at most 75 distinct azimuths: $N_{az} \geq 84$. $L_{az} \leq 75$, which yields that $N_{az} \geq L_{az}$.

Thus, there is sufficient number of Imc neurons to encode azimuthal locations, precluding the need for a combinatorial solution for selection at all location-pairs along the azimuth (involving multilobe neurons with RF lobes spread along the azimuth). Consistent with this expectation, azimuthal encoding by Imc neurons is effectively single-lobed: all lobes of a multilobe Imc neuron encode the same azimuth (Figures 2A–2C).

Optimization model for solving stimulus selection at all elevational location-pairs (Figure 4)—Conceptualizing and setting-up the model (Figure S4). In our model,

L = number distinct spatial elevations at a given azimuth encoded in our model (i.e., the number of elevations in the 'OTid' space map).

N = number of model Imc-like neurons, i.e., neurons with Imc-like anatomical projection patterns.

k_{max} = maximum number of RF lobes allowed for each model neuron.

N^* = smallest number of upto-k_{max}-lobed model neurons needed to solve selection across L elevations.

The optimization model solves for the number and positions of RF lobes of each of the N model neurons in order to achieve selection at all location-pairs. The model neurons are 'Imc-like': each of them is excited by a stimulus placed anywhere within its RF, and delivers competitive inhibition to all locations in the OTid space map outside its RF that is proportional to the strength of the stimulus (Figures S4A and S4B). Without loss of generality, we take stimulus priority = 1 unit (for all stimuli), and the proportionality constant (underlying inhibition by the Imc) to be 1. Therefore, for each stimulus, each neuron excited by that stimulus generates an inhibition of 1 unit at those locations in the OTid that are outside that neuron's RF (Figures S4A and S4B). For successful, relativepriority dependent competitive stimulus selection between stimuli presented at a given pair of locations, the net inhibition at these two locations in the OTid should be equal. For competitive selection to be solved at all location-pairs, this condition must hold for stimuli placed at any pair of all the possible ${}^{L}c_{2}$ (L choose 2) pairs of locations. The details of the setup of the optimization problem are described below.

Let X be a matrix of size $L \times N$ (Figure S4C), where the j^{th} column of the matrix corresponds to the L elevational locations encoded by the j^{th} Imc neuron in the population. The optimization problem is framed as min_X f (X; L, N), where the objective function f(X) is designed such that it achieves its minimum value (of $-L(L-1)$) for a given L only when the RFs of the model neurons solve selection at all location-pairs.

Consider two competing stimuli (of equal strength) placed at locations 1 and 2. In our scheme, we represent this by a row vector u_{1xn} = [1 1 0..0.0] (Figure S4D). The ones in the first two indices of the row vector correspond to the two locations at which the competing stimuli are placed.

Note that $X^T u^T$ results in a vector in which the j^{th} index corresponds to the number of locations that the j^{th} neuron is activated by when the two competing stimuli are placed in positions shown in a (Figure S4E).

Additionally, the matrix (X-**1**) corresponds to the suppression image of the Imc population, where **1** is a matrix vector of all ones. The j^{th} column of this matrix represents the locations to which the j^{th} Imc neuron sends inhibition in the OT space map. This is because of the inverse anatomical projections from the Imc to the OT. The product $(X\text{-}\mathbf{1})X^T u^T$ then results in a vector in which the j^{th} index corresponds to the net inhibition sent to the j^{th} location by the entire Imc population when the two competing stimuli are placed at different locations, i.e., at different positions within the row vector u (Figure S4F).

For competitive selection at these two locations, the net inhibition at these two locations in the space map of the model 'OTid' should be equal. To penalize solutions for which this is not the case, we include a cost term in the objective function that is equal to the square of difference in the inhibition at the two locations. This is written mathematically as

$$f_1(X;u,L,N) = \left(v(X-1)X^T u^T\right)^2 \quad (7)$$

where v is a row vector whose length equals that of u and nonzero indices are same as u, but with the sign of one of the 1 s flipped (in this case v = [1 1 0..0.0] or [−1 1 0..0.0]). The minimum value that f_1 can take is 0, which happens when equal inhibition is sent to both the locations at which the competing stimuli are placed (Figure S4F).

In addition to the strength of inhibition at the two locations being equal, the strength of inhibition must be strictly negative. This is because, the other possibility, of strength of inhibition at each location being zero, would not be acceptable because no inhibition would be sent to either of the two locations. To penalize solutions for which this condition is not met, we include a cost term in the objective function that is equal to the number of locations at which the inhibition is not negative. This is written mathematically as

$$f_2(X;u,\ L,\ N) = u * sign\left((X-1)X^T u^T\right) \quad (8)$$

Minimizing $f2$, therefore, ensures that inhibition is sent to both the locations. The minimum value f_2 can take is −2, when inhibition is sent to both the competing locations (Figure S4F).

Finally, we write the full objective for the location-pair (the locations in the pair are specified in the vector u) as below

$$\begin{aligned} f\left(X;u,\ L,\ N\right) &= f_1\left(X;u,\ L,\ N\right) + f_2\left(X;u,\ L,\ N\right) \quad (9)\\ &= \left(v(X-1)X^T u^T\right)^2 + u * sign\left((X-1)X^T u^T\right) \end{aligned}$$

The minimum possible value that f can take is −2.

For location invariance to be achieved, the function f should be minimized for each pair of locations at which competing stimuli can be placed. In other words, f should be minimized for all possible permutations of vector u. This can be written mathematically as

$$f(X;u,\ L,\ N) = tr\left(V(X-1)X^T U^T\ .*\ V(X-1)X^T U^T\right) + tr\left(U * sign\left((X-1)X^T U^T\right)\right) \quad (10)$$

where U is the permutation matrix of vector u (thus rows of U contain all possible location-pairs). V is the corresponding permutation matrix of vector v. $tr(Y)$ refers to the trace (sum of all the diagonal elements) of the matrix Y. Y.*Z is the Hadamard (element-wise) product between the matrices Y and Z and $sign(Y)$ is a matrix obtained by applying the element-wise sign operator to the matrix Y.

Because there are ${}^{L}c_2$ possible location-pairs (corresponding to the ${}^{L}c_2$ permutations of the vector a), the minimum value that f can achieve is $2*{}^{L}c_2 = -L(L\text{-}1)$. Thus, selection is solved at all location-pairs in our optimization model if and only if the cost function converges to the lowest possible value of $-L(L\text{-}1)$.

We add two constraints to this optimization scheme. First, we code the RFs of all the model neurons with ones (inside RF) and zeros (outside RF), a simplifying assumption (see "Model assumptions" section below for implications of this assumption). Second, we introduce a mechanism to limit the number of lobes in any model neuron to k_{max}. This is done so that, by setting $k_{max} = 3$, we would be able to match the experimentally observed constraint that there are no more than three RF lobes per Imc neuron. The first constraint is fed into the optimization problem as bounded integer constraints with bounds between 0 and 1 to make the RFs binary. The second constraint is implemented as an inequality constraint, written mathematically as

$$g(j) = k_{max} - 1_L * X_j \geq 0, \ for\ all\ j = 1, 2 \ldots N \quad (11)$$

where 1_L is a row vector of length L, and X_j is the j^{th} column of X corresponding to the RF of the j^{th} neuron. Additionally, we also test the model with $k_{max} = 10$ for some of the analyses reported in Figures 4, 5, and 7.

We solve the above nonlinear optimization problem with mixed constraints, an np-complete problem, using the '*MIDACO*' solver in MATLAB (Schlueter et al., 2012).

Estimating N*: N^* is the smallest number of model neurons needed to solve selection at all location-pairs for a given L and k_{max}, i.e., the smallest N for which the minimum value of the objective function ($-L(L\text{-}1)$) can be successfully achieved. This was estimated as follows. For each value of N from 1 to L, we ran the optimization model 1000 times (1000 runs). Any given run was said to have converged to a solution if the value of cost function did not change for 1000 successive iterations (by setting the '*evalstop*' criterion in the optimization code to 1000), thereby reaching an asymptotic value. The collection of model neuron RFs at convergence was called a 'convergent solution'. Additionally, if the convergent solution attained the value of $-L(L\text{-}1)$, then it was called an 'optimal solution'. In other words, optimal solutions are ones that converged and additionally achieve stimulus selection at all location-pairs.

N^* (for a given L and k_{max}) is, therefore, the smallest value of N for which at least one of the 1000 runs yielded an optimal solution, meaning that for $N = N^* - 1$, none of the 1000 runs yielded a solution that successfully achieved selection across all L locations.

For instance, if $k_{max} = 1$ lobe, then for all L, $N^* = L$ (Figure 4A, blue data; consistent with theoretical calculation presented in the text surrounding Figure 3). If $k_{max} = 3$ lobes and $L = 5$ elevations, all runs for all values of N from 1 to L yielded convergent solutions, but *optimal* solutions were produced only when $N \geq 4$ (Figure S5A). More generally, if $k_{max} > 1$ lobe, then for all $L > 4$, $N^* < L$ (Figure 4A; orange and black data).

Range of k_{max} values chosen for various analyses (Figure 4A onward): The specific values of k_{max} used in our simulations (Figures 4, 5, and 7) were 1, 3, and 10 lobes. The reasoning for this choice of values is described below.

k_{max} = 1 lobe corresponded to the null hypothesis of single-lobed RFs

k_{max} = 3 lobes represented Imc data (Figure 1L)

k_{max} = 10 lobes. (i) The range of elevations encoded by the OTid and the Imc is no greater than −60° to 60°, and (ii) Most individual RF-lobes have a half-max height ≥ 10° (10-percentile value of half-max height of an individual RF lobe = 10° (Figure S3G). Therefore, the number of possible distinct lobes along elevation for RFs of typical Imc neurons ≤~10 lobes (= 120°/ (10°+ 2°); with the two added degrees representing 1°spacing on either side of a lobe to separate it from abutting ones.)

Model assumptions.: Our optimization model makes two key simplifying assumptions: (a) discretized (pixelated) spatial locations, and (b) binary (on or off) RFs of the model neurons. The former assumption can be readily reconciled with biology by making the pixel size sufficiently small. Therefore, this assumption does not result in loss of generality of the model. Second, the pattern of spatial inhibition sent to the OTid space map, the key computational function required of Imc in the model, is the spatial inverse of the RF: inhibition is sent to all locations except the ones inside the RF. In other words, the spatial pattern of inhibition is, by definition, a '*binarized* spatial inverse' of the Imc RF, with the strength of delivered inhibition being proportional to the specific location within the continuous RF at which the stimulus is placed (Figures S4A and S4B). For the model, it is the pattern of inhibition that is critical, informationally speaking, rather than the variations in the strength of delivered inhibition based on the specific location within RF that a stimulus occupies (Figures S4A and S4B). (This is unlike population vector coding, where the specific values of firing rates within an RF are critical informationally (Georgopoulos et al., 1986; Lee et al., 1988; Lewis and Kristan, 1998; Ma et al., 2006)). Therefore, the continuous RF can be binarized itself (say, at the half-max, or 75%-max level) without the qualitative conclusions of the model being affected (Figures S4A and S4B). Notably, despite these simplifying abstractions of the biology by the model, we found that predictions from the model held true experimentally (Figure 6), further revealing that the model captured sufficiently well the key computational principles at play in this circuit. Consequently, it was able to provide a compelling explanation for the unusual functional properties of Imc neurons, and illuminate the neural mechanisms by which this midbrain circuit solves stimulus selection at all location-pairs.

Characterizing signature properties of optimal model solutions, and testing them in experimental data (Figures 5 and 6)

The "multilobe property"(property #1)

Model.: For each optimal solution at each (L, k_{max}, N) tested, we examined if any of the model RFs were multilobed. A model RF was said to be multilobed if it had "on" pixels that were separated by "off" pixels; two adjacent "on" pixels were treated as one lobe. For

instance, in Figure 4B, neurons #2 and #4 have one lobe each. Neuron #1 has two RF lobes and neuron #2 has 3 RF lobes. These two neurons are multilobed. Thus, this optimal model solution is said to satisfy the "multilobe property."

Data.: For each coronal Imc plane recorded, we examined if any of the neurons in that plane had multilobed RFs. Whether an RF was single or multilobed was determined using methods described in (and surrounding) Figure 1.

The "optimized lobe-overlap property " (property #2)

Model.: A multilobed model neuron that shares each of its RF lobes, but not all, with another neuron is said to satisfy this property. If every neuron in a model solution satisfies this property, the model solution itself is said to satisfy the optimized lobe-overlap property. The fraction of model solutions satisfying this property for each (L, N*) is plotted in Figure 5C (100%, in each case).

Data.: The set of neurons recorded within a given coronal plane, i.e., across all the recording sites along a dorsoventral penetration, is collectively a potential solution set for solving selection across all elevation pairs at that azimuth. (This is because of our finding that spatial azimuth is encoded topographically along the rostrocaudal axis of the Imc, and all the elevations at a given azimuth are encoded by the neurons in the coronal plane at the appropriate point along the rostrocaudal axis; Figures 2 and S3). A multilobe neuron that shares at least one of its RF lobes, but not all, with another neuron in the solution set is said to satisfy the experimentally testable version of the lobe-overlap property. To test this property in data, we first obtained the set of discrete elevational locations encoded by Imc neurons in a solution set (coronal plane). We did this by quantizing, at a resolution of 3° (to match theory and model; see main text related to Figure 3), the maximum elevation range encoded by their RFs combined. Next, an RF lobe of a multilobed Imc neuron was said to overlap with the RF of another neuron if there existed a location within the former's half-max extent that also lay within the half-max extent of the latter's RF. The fraction of multilobed Imc RFs in each coronal plane that satisfy this testable version of the optimized lobe-overlap property is shown in Figure 6C. (This testable version of the lobe-overlap property was necessary because of the inherent infeasibility of recording from all Imc neurons in a coronal section, i.e., from all the neurons in a 'solution set'. Specifically, the small mediolateral extent of the Imc (< 350 μm), coupled with the thickness of the electrode (250 μm) that was used to reliably target the deep Imc (~16 mm below brain surface), limited us to one dorsoventral penetration within a coronal section. This made recording from all Imc neurons in a given section unviable. The average # neurons recorded per section = 3.44 ± 0.47.

The "combinatorial" property (property #3)

"Assorted neural subset"feature.: Distant neurons are recruited to achieve selection for nearby locations, and nearby neurons are recruited to achieve selection for distant locations. To test for this feature, we divide the elevation range (L locations) into three parts, the upper L/3, middle L/3 and lower L/3 locations. Two locations are said to be '*nearby*' if the distance between them is ≤ L/3, and '*distant*' if the distance between them is ≥ 2L/3. Similarly, two

neurons are said to be nearby if the distance between them is ≤ (N-1)/ 3, and distant, if their distance is ≥ 2(N-1)/3. We then ask if distant neurons are recruited for a nearby location-pair (LP), and vice-versa. Since there is no meaningful functional ordering of multilobe neurons owing to the lack of topography in the encoding of elevation, we must test these questions across permutations of the ordering of Imc neurons within a solution.

Model.: First, we tested if distant neurons are recruited for a nearby location-pair. We did so by computing the following metric (Equation 12) for each (L, N*) (Figures 5E and 5F).

$$d\ (nearby\ LP) = \left[\min_{solutions}\left\{\min_{permutations}\left(\max_{nearby\ LP}(d)\right)\right\}\right] \quad (12)$$

Here, '*d*' is the maximum distance between the neurons recruited for solving selection for a given nearby location-pair in a given solution. The maximum of this across all nearby location-pairs yields the farthest distance between neurons recruited to solve selection for any nearby location-pair. The minimum of this value across permutations of neurons in the solution, and across all solutions, yields *d (nearby LP)* for that (L, N*).

For L = 5 (N* = 4), we tested this exhaustively for all possible permutations (= *factorial(4)*). However, for L = 20 (N* = 14) and L = 40 (N* = 27), the number of permutations is very large (*14!* = 8.7 ×10^{10} and *27!* = 1.08 3 10^{28}). Because it was infeasible to test all possible permutations in these cases, we tested a subset of permutations (n = 1000) that was selected randomly from the set of all the possible permutations using the '*randperm*' function in MATLAB.

For each (L, N*), we calculated the normalized minimum distance between neurons recruited for selection at distant location-pairs as shown in Equation 13, and plotted it in Figure 5F.

$$d_{norm}(nearby\ LP) = \frac{d(nearby\ LP) - d_{min}}{d_{max} - d_{min}} \quad (13)$$

Here, d_{max} (= N*−1) and d_{min} (= 1) are the maximum and minimum possible distances between neurons in a solutions set consisting of N* neurons. We found that in every case, this normalized distance was high (> 0.66; the normalized cut-off value chosen for defining 'distant' neurons).

Next, we tested if nearby neurons are recruited for a distant location-pair (Figures 5E and 5G), using a metric constructed with a logic similar to that used above:

$$d\ (distant\ LP) = \left[\max_{solutions}\left\{\max_{permutations}\left(\min_{distant\ LP}(d)\right)\right\}\right] \quad (14)$$

$$d_{norm}(distant\ LP) = \frac{d(distant\ LP) - d_{min}}{d_{max} - d_{min}} \quad (15)$$

For each (L, N*), we calculated the normalized maximum distance between neurons recruited for selection at distant LPs (Equation 15), and plotted the results in Figure 5G. We found that in every case, this normalized distance was small (< 0.33; the normalized cut-off value chosen for defining 'nearby' neurons).

Data.: For Imc neurons in each solution set (coronal plane), we obtained the range of discretized elevation values encoded as before (resolution of 3°), and then calculated the normalized minimum distance between nearby neurons and the normalized maximum distance between distant neurons using the Equations 13 and 15 above. Note that for the notions of nearby neurons and distant neurons, there need to be at least 3 neurons in the solution set so that the maximum distance is 2 and the minimum distance is 1. Out of 14 coronal planes that contained multilobe neurons, 8 had ≥ 3 neurons. The results from these 8 planes are plotted in Figure 6F.

(B) "Extensive intersection"feature.: Location-pairs occupying distant portions of space recruit shared neurons to solve selection at each pair. Two location-pairs are said occupy distant portions of (elevational) space if one location-pair lies within the upper third of the locations (upper L/3) and the other lies within the lower third of the locations (lower L/3). Since intersection between the neural subsets is independent of the ordering of the neurons, we do not need to test this for all permutations of neuron orderings.

Model.: For every optimal solution at a given (L, N*), we tested if there existed two location-pairs (a 'doublet') occupying distant portions of space such that the neural subsets recruited to solve selection at each location-pair shared at least one neuron. The fraction of optimal solutions that satisfied this property is plotted as a function of (L, N*) in Figure 5I; the fraction is uniformly 100%.

Data.: For Imc neurons in each solution set (coronal plane), we obtained the range of discretized elevation values encoded as before (resolution of 3°). We then tested if these neurons satisfied the extensive-intersection property as described for the model. Of the 14 coronal planes at which neurons were recorded, in 6 cases, the encoded locations included two location-pairs that occupied distant locations. The fraction of these 6 coronal planes that satisfied the extensive intersection property is shown in Figure 6G (100%).

Wiring and metabolic costs in the Imc-OT circuit for implementing selection at all location-pairs (Figure 7)

Wiring cost: The wiring cost incurred by the Imc to implement selection at all location-pairs is estimated as the cost of generating axonal projections ('wires') between each Imc neuron and each of its target OTid neurons. This cost depends both on the number of locations that each neuron must suppress and the number of neurons in the population.

Assuming that the lengths of wires from Imc to each OTid neuron is approximately equal (say 1 unit each, without loss of generality), we can estimate the total wiring length and consequently the total wiring cost using Equation 16 below (see Chen et al., 2006).

$$Wiring\ Cost\left(L, N^*, k_{max}\right) = \left(\sum_{i=1}^{N^*} (\ \#\ \text{Locations suppressed by neuron } i)\right) \wedge p \quad (16)$$

The summation is the total wiring length of all the wires from the Imc neurons to the OTid population. 'p' is a power term such that typically 1 < p < 4 (see Chen et al., 2006). This quantity is computed for each optimal solution (obtained over the 1000 runs) for a given (L, N*, k_{max}) triplet, and the results are plotted in Figure 7A.

Metabolic cost: The metabolic cost incurred by the Imc to implement selection at all location-pairs is estimated as the cost of generating and broadcasting spikes to the OTid to achieve competitive suppression. This depends on the number of neurons activated by a stimulus at each of the L locations, as well as the number of OTid locations to which each activated neuron delivers inhibition. If the cost of suppressing one OTid location using 1 spike is 1 unit, then the total metabolic cost for the circuit for a given firing rate f is given by Equation 17 below (using a similar formula as for wiring cost).

$$Metabolic\ cost\left(L, N^*, k_{max}, f\right) = \left(\frac{f}{L}\sum_{j=1}^{L}\sum_{i=1}^{N^*} (\ \#\ \text{Locations suppressed by neuron } i \text{ when stimulus is placed at location})\right) \wedge q \quad (17)$$

Note that when the stimulus is placed at location *j*, the term in the inner summation is non-zero only for activated neurons. 'q' is a power term chosen such that 1 < q < 4 (similar to the wiring cost). This quantity is computed for each optimal solution (obtained over the 1000 model runs) for a given (L, N^*, k_{max}, $f = 10\ Hz$), and the results plotted in Figure 7B.

Total cost: The total cost for any solution is calculated as a weighted combination of the wiring cost (weight = α) and the metabolic cost (weight = β) as given in Equation 18 below.

$$Total\ cost\left(L, N^*, k_{max}, f\right) = \left(\alpha * Wiring\ cost\left(L, N^*, k_{max}\right)\right) + \left(\beta * Metabolic\ cost\left(L, N^*, k_{max}, f\right)\right) \quad (18)$$

Therefore, there are five parameters (α; p; β; q and f) in the computation of the total cost. The results are plotted for $\alpha = 20$; $p = 2{:}5$; $\beta = 80$; $q = 2{:}42$ and for firing rates of $f = 10$ Hz (thin black line) and $f = 80$ Hz (thick black line) in Figure 7C.

QUANTIFICATION AND STATISTICAL ANALYSIS

All analyses were carried out with custom MATLAB code. Parametric or non-parametric statistical tests were applied based on whether the distributions being compared were Gaussian or not, respectively (Lilliefors test of normality). The Holm-Bonferroni correction was used to account for multiple comparisons. Data shown as a ± b refer to mean ± s.e.m, unless specified otherwise. The '*' symbol indicates significance at the 0.05 level (after corrections for multiple comparisons, if applicable). Correlations between RF centers (azimuth) and electrode measurement positions (rostrocaudal/ dorsoventral) were tested using Spearman's rank correlation coefficient (corr command in MATLAB with the Spearman option).

Supplementary Material

Refer to Web version on PubMed Central for supplementary material.

ACKNOWLEDGMENTS

This work was supported by funding from NIH grant R01 EY027718. We are grateful to Drs. James Knierim and Daniel O'Connor for feedback.

REFERENCES

Bala ADS, Spitzer MW, and Takahashi TT (2003). Prediction of auditory spatial acuity from neural images on the owl's auditory space map. Nature 424, 771–774. [PubMed: 12917684]

Carrasco M, and Frieder KS (1997). Cortical magnification neutralizes the eccentricity effect in visual search. Vision Res. 37, 63–82. [PubMed: 9068831]

Chen BL, Hall DH, and Chklovskii DB (2006). Wiring optimization can relate neuronal structure and function. Proc. Natl. Acad. Sci. USA 103, 4723–4728. [PubMed: 16537428]

Fecteau JH, and Munoz DP (2006). Salience, relevance, and firing: a priority map for target selection. Trends Cogn. Sci 10, 382–390. [PubMed: 16843702]

Fee MS, Mitra PP, and Kleinfeld D (1996). Automatic sorting of multiple unit neuronal signals in the presence of anisotropic and non-Gaussian variability. J. Neurosci. Methods 69, 175–188. [PubMed: 8946321]

García-Cabezas MA, John YJ, Barbas H, and Zikopoulos B (2016). Distinction of neurons, glia and endothelial cells in the cerebral cortex: an algorithm based on cytological features. Front. Neuroanat 10, 107. [PubMed: 27847469]

Georgopoulos AP, Schwartz AB, and Kettner RE (1986). Neuronal population coding of movement direction. Science 233, 1416–1419. [PubMed: 3749885]

Goddard CA, Huguenard J, and Knudsen E (2014). Parallel midbrain microcircuits perform independent temporal transformations. J. Neurosci 34, 8130–8138. [PubMed: 24920618]

Graybiel AM (1978). A satellite system of the superior colliculus: the parabigeminal nucleus and its projections to the superficial collicular layers. Brain Res. 145, 365–374. [PubMed: 638795]

Hafting T, Fyhn M, Molden S, Moser MB, and Moser EI (2005). Microstructure of a spatial map in the entorhinal cortex. Nature 436, 801–806. [PubMed: 15965463]

Jiang ZD, King AJ, and Moore DR (1996). Topographic organization of projection from the parabigeminal nucleus to the superior colliculus in the ferret revealed with fluorescent latex microspheres. Brain Res. 743, 217–232. [PubMed: 9017249]

Knudsen EI (1982). Auditory and visual maps of space in the optic tectum of the owl. J. Neurosci 2, 1177–1194. [PubMed: 7119872]

Knudsen EI (2007). Fundamental components of attention. Annu. Rev. Neurosci 30, 57–78. [PubMed: 17417935]

Kruskal JB, Jr. (1956). On the shortest spanning subtree of a graph and the traveling salesman problem. Proc. Am. Math. Soc 7, 48–50.

Lawler EL, Lenstra JK, Rinnooy Kan AHG, and Shmoys DB (1985). The traveling salesman problem. A guided tour of combinatorial optimization. J. Oper. Res. Soc 37, 536.

Lee C, Rohrer WH, and Sparks DL (1988). Population coding of saccadic eye movements by neurons in the superior colliculus. Nature 332, 357–360. [PubMed: 3352733]

Lewis JE, and Kristan WB, Jr. (1998). A neuronal network for computing population vectors in the leech. Nature 391, 76–79. [PubMed: 9422507]

Li DP, Xiao Q, and Wang SR (2007). Feedforward construction of the receptive field and orientation selectivity of visual neurons in the pigeon. Cereb. Cortex 17, 885–893. [PubMed: 16723406]

Lovejoy LP, and Krauzlis RJ (2010). Inactivation of primate superior colliculus impairs covert selection of signals for perceptual judgments. Nat. Neurosci 13, 261–266. [PubMed: 20023651]

Ma WJ, Beck JM, Latham PE, and Pouget A (2006). Bayesian inference with probabilistic population codes. Nat. Neurosci 9, 1432–1438. [PubMed: 17057707]

Mao D, Kandler S, McNaughton BL, and Bonin V (2017). Sparse orthogonal population representation of spatial context in the retrosplenial cortex. Nat. Commun 8, 243. [PubMed: 28811461]

Marín G, Salas C, Sentis E, Rojas X, Letelier JC, and Mpodozis J (2007). A cholinergic gating mechanism controlled by competitive interactions in the optic tectum of the pigeon. J. Neurosci 27, 8112–8121. [PubMed: 17652602]

McPeek RM, and Keller EL (2004). Deficits in saccade target selection after inactivation of superior colliculus. Nat. Neurosci 7, 757–763. [PubMed: 15195099]

Meredith MA, and Stein BE (1986). Visual, auditory, and somatosensory convergence on cells in superior colliculus results in multisensory integration. J. Neurophysiol 56, 640–662. [PubMed: 3537225]

Mysore SP, and Knudsen EI (2013). A shared inhibitory circuit for both exogenous and endogenous control of stimulus selection. Nat. Neurosci 16, 473–478. [PubMed: 23475112]

Mysore SP, Asadollahi A, and Knudsen EI (2010). Global inhibition and stimulus competition in the owl optic tectum. J. Neurosci 30, 1727–1738. [PubMed: 20130182]

Mysore SP, Asadollahi A, and Knudsen EI (2011). Signaling of the strongest stimulus in the owl optic tectum. J. Neurosci 31, 5186–5196. [PubMed: 21471353]

Olshausen BA, and Field DJ (1997). Sparse coding with an overcomplete basis set: a strategy employed by V1? Vision Res. 37, 3311–3325. [PubMed: 9425546]

Rizzolatti G, Camarda R, Grupp LA, and Pisa M (1974). Inhibitory effect of remote visual stimuli on visual responses of cat superior colliculus: spatial and temporal factors. J. Neurophysiol 37, 1262–1275. [PubMed: 4436699]

Rodriguez A, and Laio A (2014). Machine learning. Clustering by fast search and find of density peaks. Science 344, 1492–1496. [PubMed: 24970081]

Schlueter M, Gerdts M, and Ruckmann JJ (2012). A numerical study of MIDACO on 100 MINLP benchmarks. Optimization 61, 873–900.

Sereno MI, and Ulinski PS (1987). Caudal topographic nucleus isthmi and the rostral nontopographic nucleus isthmi in the turtle, Pseudemys scripta. J. Comp. Neurol 261, 319–346. [PubMed: 3611415]

Sicard G, and Holley A (1984). Receptor cell responses to odorants: similarities and differences among odorants. Brain Res. 292, 283–296. [PubMed: 6692160]

Sridharan D, Boahen K, and Knudsen EI (2011). Space coding by gamma oscillations in the barn owl optic tectum. J. Neurophysiol 105, 2005–2017. [PubMed: 21325681]

Tibshirani R, Walther G, and Hastie T (2001). Estimating the number of clusters in a dataset via the gap statistic. J. R. Stat. Soc. B 63, 411–423.

Towse BW, Barry C, Bush D, and Burgess N (2013). Optimal configurations of spatial scale for grid cell firing under noise and uncertainty. Philos. Trans. R. Soc. Lond. B Biol. Sci 369, 20130290.

Treisman AM, and Gelade G (1980). A feature-integration theory of attention. Cognit. Psychol 12, 97–136. [PubMed: 7351125]

Wang YC, and Frost BJ (1991). Visual response characteristics of neurons in the nucleus isthmi magnocellularis and nucleus isthmi parvocellularis of pigeons. Exp. Brain Res 87, 624–633. [PubMed: 1783031]

Wang Y, Major DE, and Karten HJ (2004). Morphology and connections of nucleus isthmi pars magnocellularis in chicks (*Gallus gallus*). J. Comp. Neurol 469, 275–297. [PubMed: 14694539]

Wang Y, Luksch H, Brecha NC, and Karten HJ (2006). Columnar projections from the cholinergic nucleus isthmi to the optic tectum in chicks (*Gallus gallus*): a possible substrate for synchronizing tectal channels. J. Comp. Neurol 494, 7–35. [PubMed: 16304683]

Yilmaz M, and Meister M (2013). Rapid innate defensive responses of mice to looming visual stimuli. Curr. Biol 23, 2011–2015. [PubMed: 24120636]

Highlights

- Imc, a midbrain inhibitory nucleus, encodes visual space with multilobed RFs
- Such coding of space by the owl Imc is necessitated by scarcity of Imc neurons
- It results in combinatorially optimized inhibition for stimulus selection
- This solves stimulus selection at all location pairs while minimizing neural costs

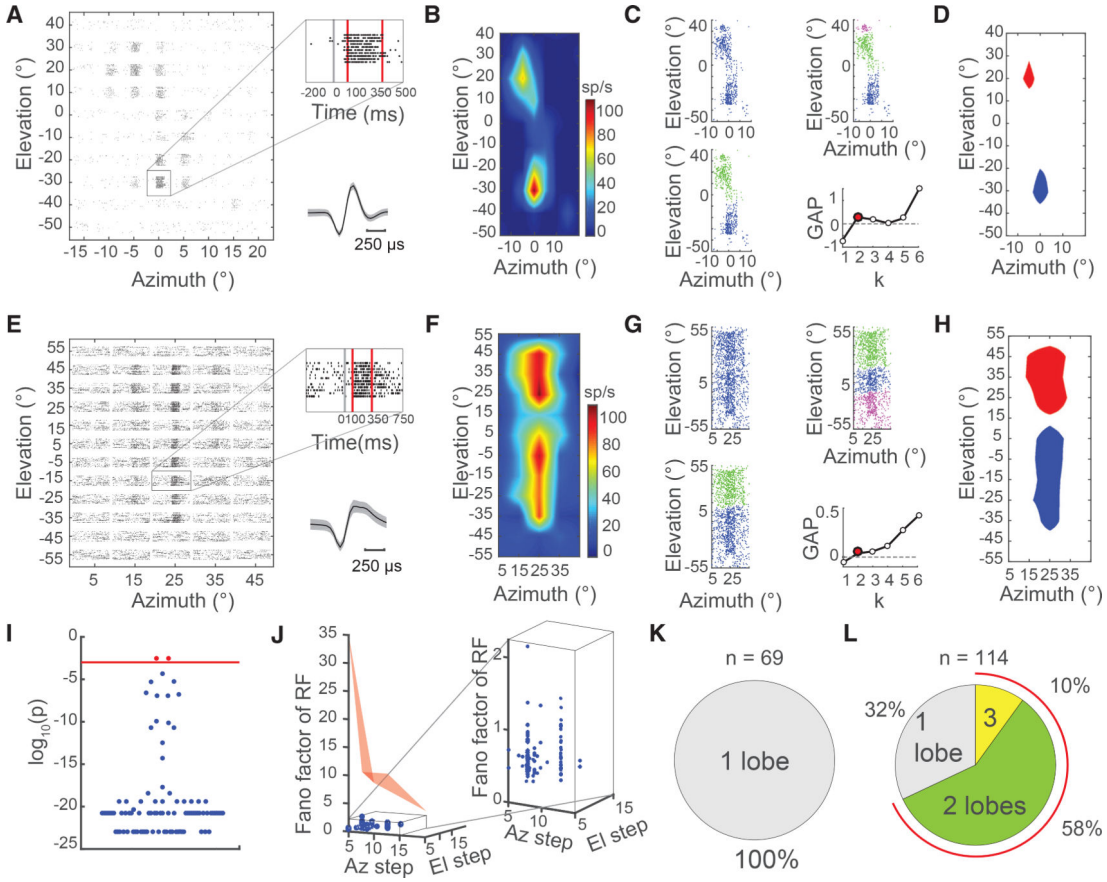

Figure 1. Visual Receptive Fields of Imc Neurons Have Multiple Distinct Response Fields (Lobes)

(A) 2D visual receptive field (RF) of Imc neuron: raster plot of neuron's responses to visual stimulus presented at different spatial locations. Inset top: gray line, stimulus onset; red lines, time window used to calculate firing rate; evoked firing rates in Imc were high (median, 76.5 Hz; n = 114 neurons). Inset bottom: average spike waveform for neuron in (A); identified as high-quality unit (STAR Methods); mean (black) ± SD (gray).

(B) Color-coded firing rate map corresponding to (A).

(C) Rate map in (B) re-plotted as distribution of points in a 2D plane and subjected to spatial clustering (STAR Methods). Shown are the best single (top left), best two (top right), and best three clusters (bottom left) fitted to the data using the density peaks clustering method (Rodriguez and Laio, 2014) (Figure S2C; STAR Methods). Bottom right: plot of GAP statistic, a robust model selection metric, against the number of clusters (k) fitted to data (Tibshirani et al., 2001) (STAR Methods). Red point: statistically optimal number of clusters (k*), identified as the smallest k for which GAP exceeds zero; here k* = 2 (STAR Methods) (Tibshirani et al., 2001).

(D) Half-max extents of these two optimal RF clusters (lobes).

(E–H) Same as (A)–(D), but for a different Imc neuron.

(I) Plot of p values (logarithmic scale) obtained from separability testing for each sorted unit; one-way ANOVA followed by correction for multiple comparisons(STAR Methods). p value < 0.05 (blue data): units that are deemed "well separated" from co-recorded units as well as outliers (n = 114). Red data: units not well separated form cohort.

(J) Effect of neuronal response variability and spatial sampling step size on number of RF lobes detected in a simulated single-lobed RF; Monte Carlo analysis(Figure S2G; STAR Methods). Red area: Fano factor and step size pairs yielding >5% rate of misidentifying single-lobed RF as multilobed. Blue data: experimentally recorded Imc neurons (n = 114). (K) Summary of number of RF lobes across 69 OT neurons. See also Figures S1 and S2. (L) Summary of number of RF lobes across 114 Imc neurons.

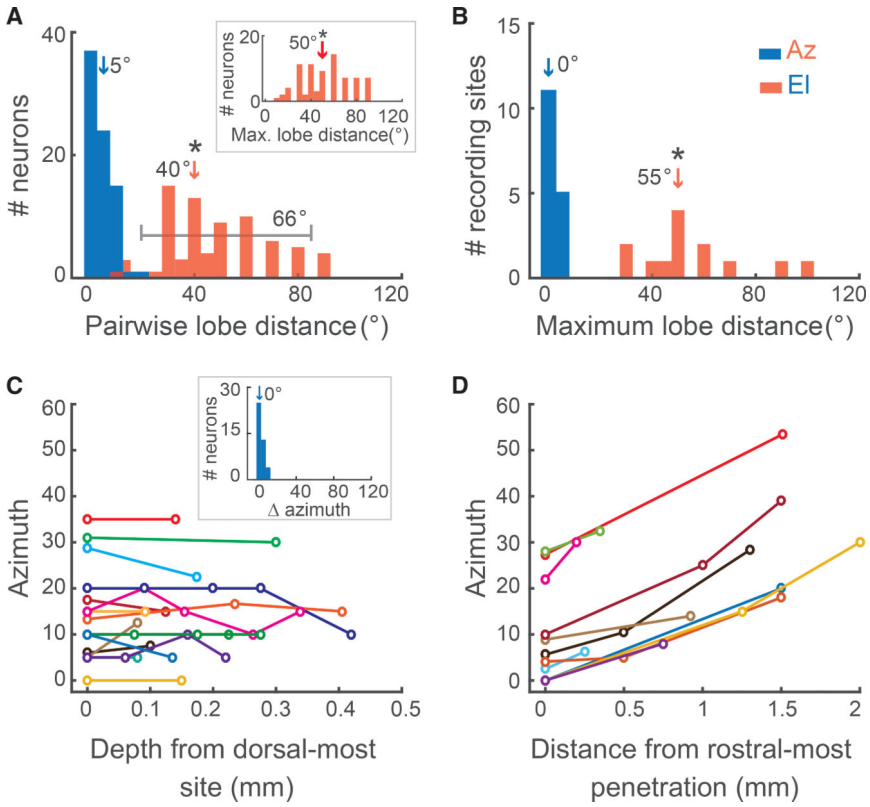

Figure 2. RF Lobes of Multilobe Imc Neurons Are Distributed along Elevation but Not Azimuth, and RFs Are Organized Topographically in Azimuth, but Not Elevation

(A) Histograms of pairwise distance between centers of RF lobes of individual multilobed neurons (STAR Methods). Blue: azimuthal distance; red: elevational distance; marked range: 5th to 95th percentile range of red data; large range indicates arbitrary spacing of RF lobes. Arrows: median values; *: median significantly different from 0 ($p = 0.17$, azimuth; $p < 0.05$, elevation; one-tailed rank sum tests). Inset: histogram of maximum elevational distance between centers of RF lobes of an individual multilobed neuron. Arrow: median value; significantly different from 0 ($p < 0.05$, one-tailed rank sum test); large median indicates widely distributed RF lobes.

(B)Histograms of maximum distances between centers of RF lobes of multilobed neurons sorted from individual recording sites (STAR Methods); conventions as in (A); $p = 0.65$ for azimuth; one-tailed rank sum test, $p < 0.05$ for elevation; one-tailed t test.

(C) Plot of average azimuthal center of a recording site against the dorsoventral position of the site within the Imc (STAR Methods); colors: different penetrations. Inset: data re-plotted as histogram of pairwise differences in the azimuthal centers of recording sites along a dorsoventral penetration ($p = 0.18$, one-tailed rank sum test). (D) Plot of average azimuthal "center" of a dorsoventral penetration against the rostrocaudal position of electrode in the Imc in that recording session (STAR Methods). Colors: different recording sessions; Spearman correlation = 1 in each case. See also Figure S3.

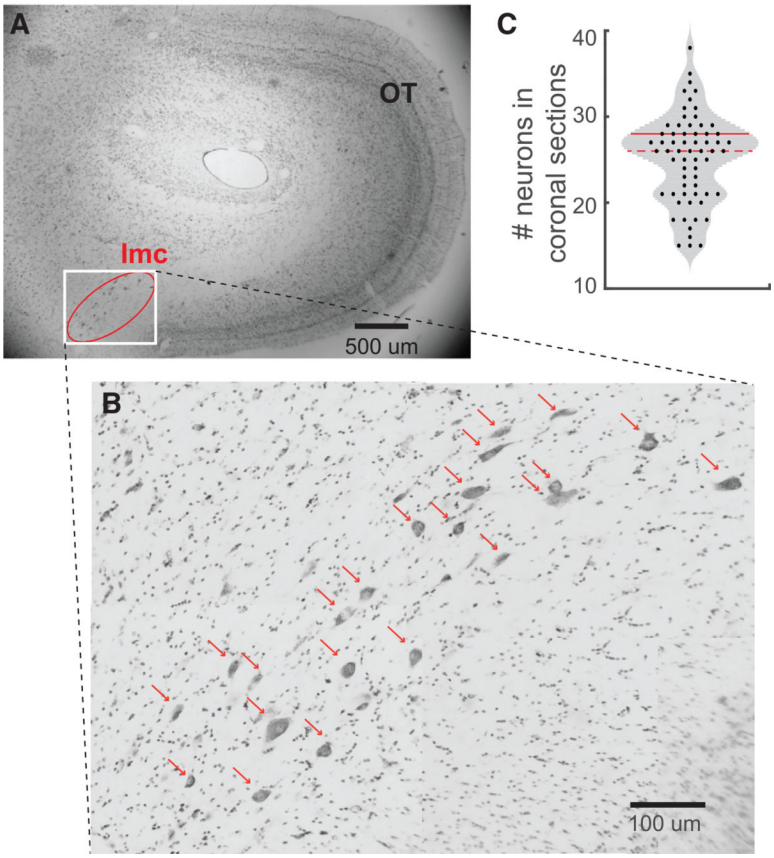

Figure 3. Imc Encodes Elevations with a Sparse Number of Neurons

(A) Coronal section of owl midbrain showing Imc and OT.

(B) Zoomed-in image showing individual, Nissl-stained, Imc somata (arrow-heads); 22 somata in this section. The zoomed-in image was obtained by stitching 5 images (each taken at 40× magnification) with overlapping fields of view at the edges.

(C) Violin plot showing number of Imc somata per coronal section; each dot,one section; n = 64 sections across two owls. Dashed line: median (26 neurons); solid line: 75th percentile (28 neurons).

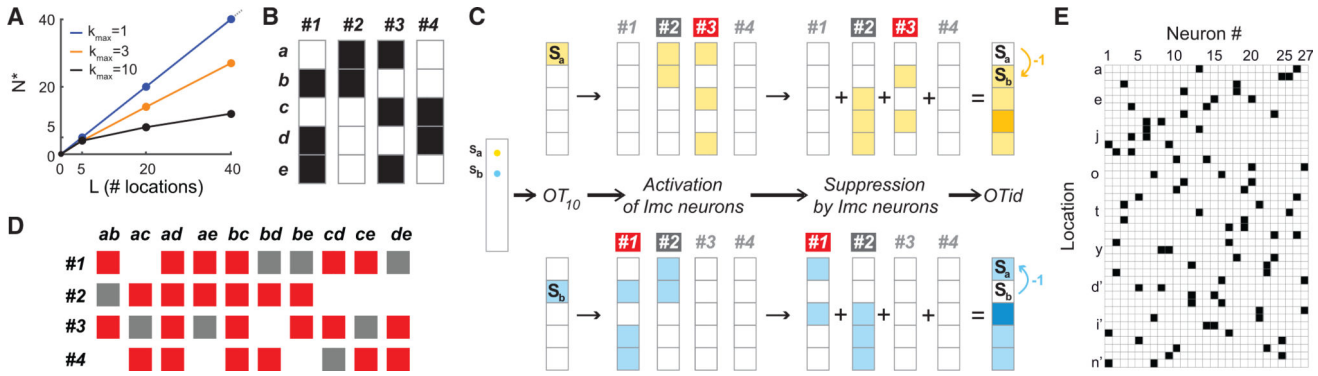

Figure 4. Example Optimal Solution from Model Illustrates Stimulus Selection at All Location Pairs with an Under-Complete Set of Neurons

(A) Summary plot showing the fewest number of neurons (N*) needed by model to solve selection across all locations for different numbers of locations (L) (Figure S5A; STAR Methods). k_{max}: maximum number of RF lobes allowed for each neuron (STAR Methods).

(B–D) Illustration of selection at all possible location pairs by an optimal model solution for L = 5 locations (numbered a–e) and N = 4 neurons (numbered #1–#4).

(B) The four RFs in the optimal solution. Shaded areas: RF of neuron; two neurons have multilobed RFs (#1, two lobes; #3, three lobes).

(C) Optimal solution in (B) implements selection between stimuli S_a and S_b at location pair *ab* (extreme left). S_a and S_b are of equal priority (1 unit for simplicity). Top row: information flow through the model OT_{10}-Imc-OTid circuit triggered by S_a. First column: activation of OT_{10} space map. Second column: activation of individual Imc neurons. Third column: suppression pattern generated by each activated Imc neuron (spatial inverse of the neuron's RF; consistent with published anatomical results; Figures S1B–S1E [Wang et al., 2004]). Fourth column: combined pattern of suppression in the OTid. Dark colors: 2 units of suppression; light colors: 1 unit (STAR Methods). Curved arrow: net suppression driven by S_a location b. Dark-gray shading: "activated" neuron (#2); defined as a neuron driven by S_a but that does not send inhibition to location b. Red shading: "recruited" neuron (#3); defined as activated neuron that sends inhibition to location b, thereby involved in selection for location pair *ab*. Bottom row: same as top row, but for stimulus S_b.

(D) Selection matrix summarizing implementation of selection at all location pairs by optimal model solution in (A). Columns: ten possible location pairs; rows: the four neurons. In each column: dark-gray, activated neurons; red, recruited neurons; blank, neurons not activated by either stimulus.

(E) Example optimal solution for (L, k_{max}, N*) = (40, 3, 27). Black pixels: locations inside neurons' RF; white pixels, locations outside neurons' RF.

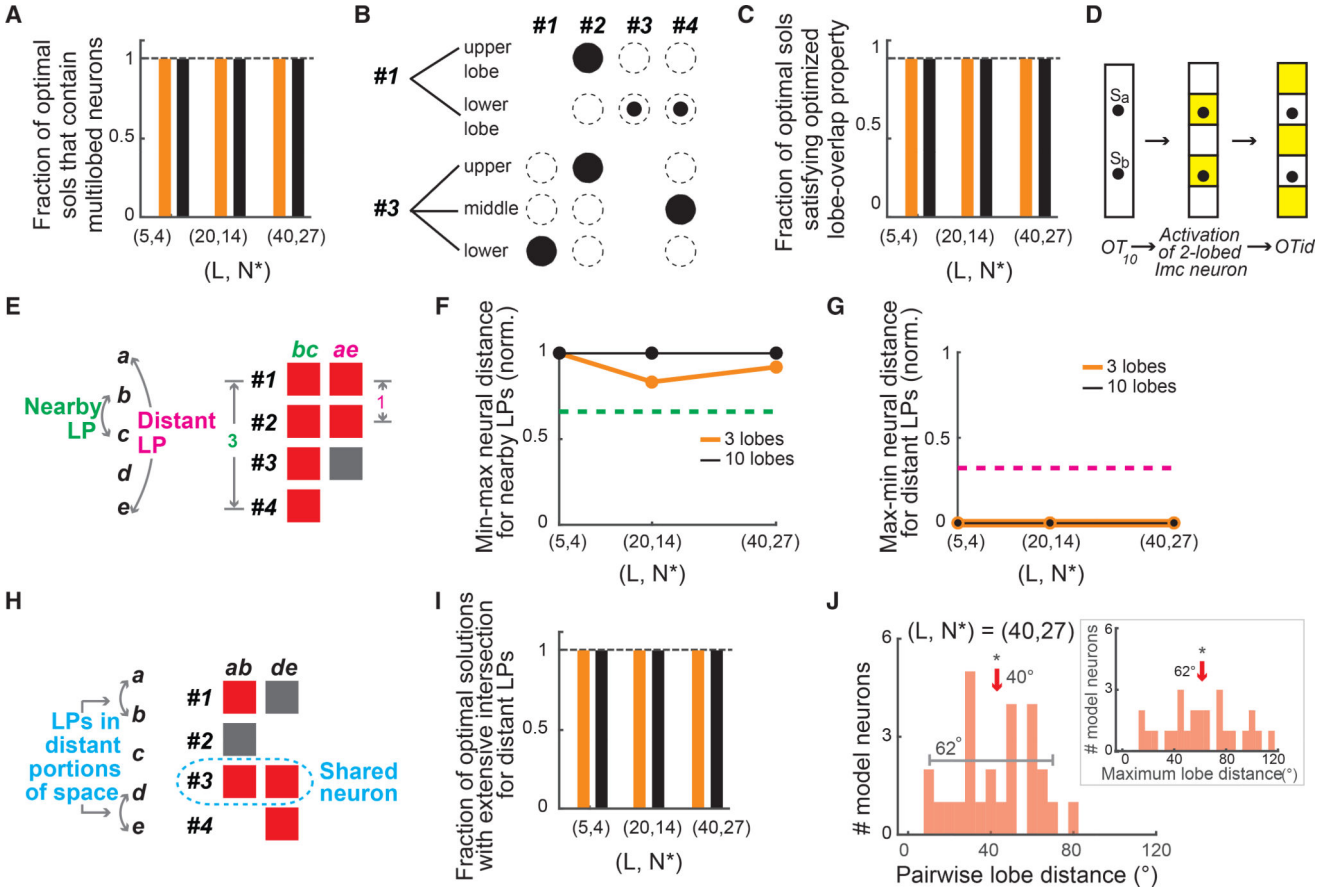

Figure 5. Model Solutions Reveal Combinatorially Optimized Inhibition Strategy for Stimulus Selection at All Location Pairs with an Under-Complete Set of Neurons

Quantification of signature properties of combinatorially optimized inhibition for optimal model solutions.

(A) Signature property #1 (multilobe neurons). Fraction of optimal model solutions that had multilobed Imc neurons for all (L, N*) pairs; orange bars, k_{max} = 3; black bars, k_{max} = 10.

(B–D) Signature property #2 (optimized lobe overlap; see text).

(B) Illustration of property for example optimal solution in Figure 4B. Top row: multilobe neuron #1 in Figure 4B shares upper, but not lower lobe with neuron #2, and shares lower, but not upper lobe with neurons #3 and #4. Bottom row: similar, but for multilobe neuron #3. (C) Fraction of optimal model solutions that satisfy the “optimized lobe overlap” property; conventions as in (A).

(D) Schematic illustrating need for the optimized lobe overlap property of multilobed Imc neurons. Shown is a two-lobed Imc neuron (middle). When stimuli S_a and S_b both occur within the RF of this “Imc” neuron (left), the resulting zone of suppression generated by this Imc neuron in the OTid would spare both stimuli (right); selection for this location pair would not be achievable by just this neuron.

(E–J) Signature property #3 (combinatorial inhibition; see text). (E–J) “Assortedness” feature.

(E)Illustration of this feature for example optimal solution in Figure 4B. Left panel: locations *a*–*e*. Right panel: patterns of neurons activated and recruited to solve selection for

indicated location pairs (LPs); extracted from selection matrix in Figure 4D. Location pair bc involves nearby locations (left panel), but recruits distant neurons to solve selection (right panel; #1 and #4; distance = 3, yielding normalized distance of 1, the largest possible value; STAR Methods); conversely, distant location pair ae recruits nearby neurons (#1 and #2; distance = 1, yielding normalized distance of 0, the smallest possible value; STAR Methods).

(F)Summary plot showing that distant neurons are recruited for selection at nearby locations. Plotted is the normalized distance between neurons recruited for solving selection at nearby locations, termed “min-max” distance. This is the minimum, taken across optimal solutions and their permutations, of the maximum normalized distance between neurons in a solution recruited for solving selection at nearby locations. Green dashed line: normalized distance cutoff to be exceeded for neurons to be termed “distant” (0.66; STAR Methods) and “nearby” neurons (magenta; 0.33; STAR Methods).

(G) Summary plot showing that nearby neurons are recruited for selection at distant locations. Plotted is the normalized distance between neurons recruited for solving selection at distant locations, termed “max-min” distance. This is the maximum, taken across optimal solutions and their permutations, of the minimum normalized distance between neurons in a solution recruited for solving selection at distant locations. Magenta dashed line: normalized distance cutoff to not be exceeded for neurons to be termed “nearby” (0.33; STAR Methods).

(H–J) “Extensive intersection” feature.

(H) Illustration of this feature for example optimal solution in Figure 4B: location pairs occupying distant portions of space (left panel) recruit intersecting neural subsets to solve selection (right panel; STAR Methods). See also Figures S5 and S6.

(I) Fraction of optimal model solutions that satisfy the extensive intersection feature (STAR Methods; conventions as in A).

(J) Lobes of neurons in model solutions were arbitrarily placed and widely spread. Histogram of pairwise distance between centers of RF lobes of individual multilobed neurons for a randomly selected model solution for (L, k_{max}, N*) = (40, 3, 27); marked range: 5th to 95th percentile range of red data; large range indicates arbitrary spacing of RF lobes. Inset: histogram of maximum distance between centers of RF lobes of a multilobed neuron, for the same model solution.Red arrows: median values; * medians significantly different from 0 ($p < 0.001$, one-tailed rank sum test); large median indicates widely distributed RF lobes.

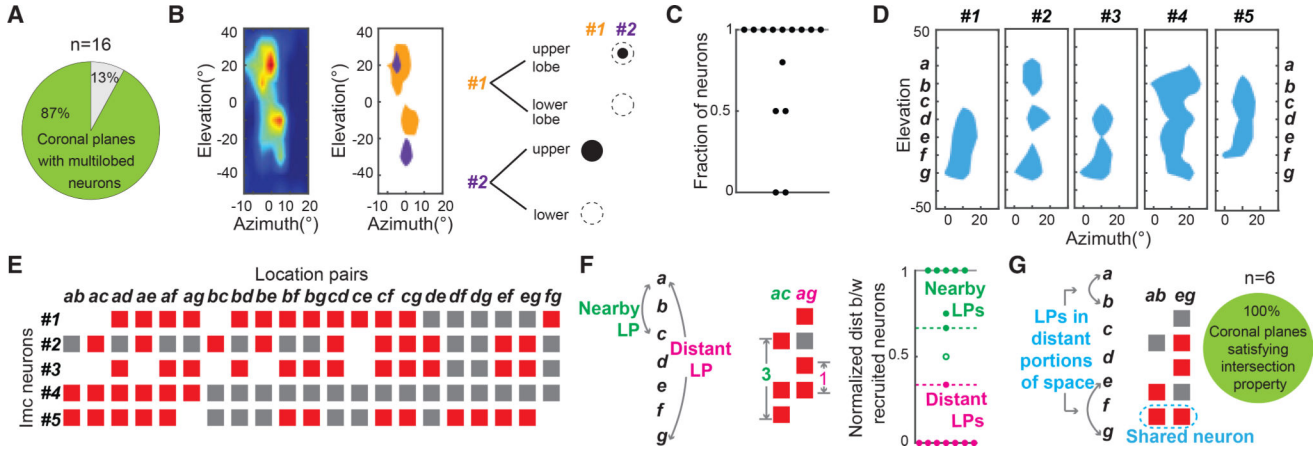

Figure 6. Experimental Validation of Combinatorially Optimized Inhibition in the Imc

(A) Signature property #1: pie chart summary of fraction of Imc coronal planes tested that contained multilobed neurons (87% = 14/16 planes; also Figures S3E and S3F).

(B and C) Signature property #2.

(B) Left: rate map of RF of another Imc neuron sorted from the same recording site as the neuron in Figures 1A–1D. (Only these two neurons were recorded in this Imc coronal plane.) Middle: half-max of RFs of neurons in Figure 1 (purple; reproduced from Figure 1D) and Figure 6B, left (orange). Right: for each neuron, the upper RF lobe, but not lower one, shows overlap, satisfying the testable lobe overlap property (see text); conventions as in Figure 5B.

(C)Fraction of multilobe neurons in each coronal plane satisfying the testable version of lobe overlap property; dot, coronal plane; median fraction = 1.

(D–F) Signature property #3.

(D)RFs (half-max) of all Imc neurons recorded within an example coronal plane. *a–g* are seven (discretized) spatial locations encoded by these neurons (STAR Methods).

(E) Selection matrix showing combinatorial activation of recorded neurons for selection at different location pairs; conventions as in Figure 4D.

(F) Two left panels: illustration of assortedness feature for example in (D); conventions as in Figure 5E (STAR Methods). Right: summary of this feature across Imc coronal planes; only those planes containing ≥ 3 Imc neurons each were testable (8/14; STAR Methods) Dashed lines: distance cutoffs for “distant” neurons (green; 0.66) and “nearby” neurons (magenta; 0.33; STAR Methods). Filled circles: Imc coronal planes that satisfied these cutoff criteria; ≥7/8 in each case (STAR Methods).(G) Left: illustration of “extensive intersection” feature for example in (D); conventions as in Figure 5H. Right: pie chart summary of this feature across coronal planes (100% exhibited the feature; 6/6). Note that this feature was testable only for those planes for which the recorded neurons encoded location pairs occupying distant portions of space (6/14; STAR Methods).

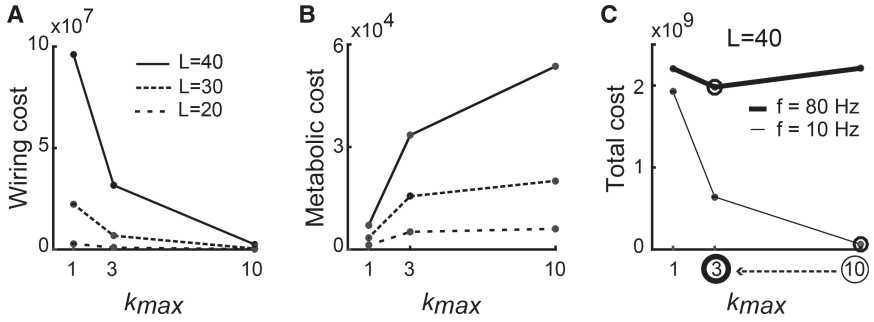

Figure 7. Metabolic and Wiring Costs for Stimulus Selection at All Possible Location Pairs

(A) Wiring cost plotted as a function of the maximum number of Imc RF lobes allowed (k_{max}); calculated across optimal model solutions (STAR Methods). Values of k_{max} examined along x axis are particularly relevant to the Imc: k_{max} = 1 corresponds the single-lobed case, k_{max} = 3 to the experimentally determined value in the owl Imc, and k_{max} = 10 to the practical upper bound on the number of possible RF lobes (based on the functional properties of Imc neurons; STAR Methods and Figure 1L).

(B) Metabolic cost as a function of k_{max} (STAR Methods).

(C) Schematic showing total cost (weighted combination of A and B) for Imc circuit to solve selection at all location pairs for L = 40 at low average firing rates (thin line, 10 Hz), and high average firing rates (thick line, 80 Hz; STAR Methods); weights used for combining wiring and metabolic costs were identical for the low and high firing rate cases. Circled values along x axis (and corresponding large dots) indicate the optimal k_{max} values at the two firing rate levels. Results demonstrate left shift of optimal k_{max} with increasing firing rates (STAR Methods; the specific values of optimal k_{max} yielded by this analysis, and shown here, are incidental to the choice of the values of relative weights, and not particularly informative by themselves.) In all cases, mean ± SD values are plotted; SD values smaller than size of dots.